Editors' Suggestion

# Interacting topological quantum chemistry of Mott atomic limits

Martina O. Soldini [1,*] Nikita Astrakhantsev [1] Mikel Iraola [2,3] Apoorv Tiwari [4] Mark H. Fischer [1] Roser Valentí [5] Maia G. Vergniory [2,6] Glenn Wagner [1] and Titus Neupert [1]

[1]*University of Zurich, Winterthurerstrasse 190, 8057 Zurich, Switzerland*
[2]*Donostia International Physics Center, 20018 Donostia-San Sebastian, Spain*
[3]*Department of Physics, University of the Basque Country UPV/EHU, 48080 Bilbao, Spain*
[4]*Department of Physics, KTH Royal Institute of Technology, Roslagstullsbacken 21, 114 21 Stockholm, Sweden*
[5]*Institut für Theoretische Physik, Goethe-Universität Frankfurt, 60438 Frankfurt am Main, Germany*
[6]*Max Planck Institute for Chemical Physics of Solids, 01187 Dresden, Germany*

(Received 28 September 2022; accepted 24 April 2023; published 29 June 2023)

Topological quantum chemistry (TQC) is a successful framework for identifying (noninteracting) topological materials. Based on the symmetry eigenvalues of Bloch eigenstates at maximal momenta, which are attainable from first principles calculations, a band structure can either be classified as an *atomic limit*, in other words adiabatically connected to independent electronic orbitals on the respective crystal lattice, or it is topological. For interacting systems, there is no single-particle band structure and hence, the TQC machinery grinds to a halt. We develop a framework analogous to TQC, but employing $n$-particle Green's function to classify interacting systems. Fundamentally, we define a class of interacting reference states that generalize the notion of atomic limits, which we call *Mott atomic limits*, and are symmetry protected topological states. Our formalism allows to fully classify these reference states (with $n = 2$), which can themselves represent symmetry protected topological states. We present a comprehensive classification of such states in one dimension and provide numerical results on model systems. With this, we establish Mott atomic limit states as a generalization of the atomic limits to interacting systems.

DOI: 10.1103/PhysRevB.107.245145

## I. INTRODUCTION

Topological quantum matter harbors universal and robust physical phenomena that are appealing for fundamental research as well as for applications [1–5]. The experimental identification of topological materials can be challenging, which may explain why topological insulators have only been discovered following theoretical predictions [6,7], despite decades of semiconductor research [8,9]. Since these discoveries, the notion of topological states has been considerably refined, starting from the 10-fold way classification [10,11], via the inclusion of spatial symmetries in topological crystalline insulators [12], to the concepts of fragile [13–15] and delicate [16] topology. These concepts have also been extended to other types of systems, beyond electronic materials, such as magnons [17,18] and optical excitations [19], to name a few. In parallel, theoretical methods have been developed to predict such topological phases in real materials. Aided by density functional theory calculations, so-called symmetry indicators [20,21] and the more comprehensive framework of topological quantum chemistry (TQC) has allowed to identify large numbers of candidate topological materials [22–26].

The principle underlying TQC is to relate *atomic limits* (ALs), defined by placing electrons on (maximal) Wyckoff positions of a crystallographic space group, to representations of a set of electronic bands in momentum space [22,24,27,28]. Independent of these considerations, one can obtain the representation of a set of bands for a material of interest from first principles band structure calculations. One says that ALs *induce* band representations. The efficient identification of band representations is obtained by listing the irreducible representations (irreps) of Bloch states at maximal momentum points in the Brillouin zone. Composing multiple ALs in the real space unit cell of a crystal corresponds to adding band representations in momentum space with positive integer coefficients. The generators of this space of band representations are called elementary band representations. Importantly, the AL-generated band representations do not span the space of all the possible band structures.

The key statement of TQC is enclosed in the following: If the representation of the bands of a given material does not admit a decomposition in terms of elementary band representations (with positive integer coefficients), the material realizes a topological state. Note that the converse is not true [15,29,30]: A nonmagnetic system in space group $C_1$ may for instance be a three-dimensional (3D) topological insulator protected by time-reversal symmetry (TRS), but in this low-symmetry space group there are no nontrivial irreps that could be used to differentiate between distinct band representations.

The TQC framework is fundamentally limited in its formulation to noninteracting systems and can thus only distinguish topological and trivial systems well described in the single-particle approximation. Topological insulators are protected by their gap and therefore, weak interactions will not destroy these phases and TQC might be applicable even with interactions. However, interactions can lead to entirely new

*Corresponding author: msoldi@physik.uzh.ch

 ©2023 American Physical Society

topological phases that are not adiabatically connected to any noninteracting limit [31–33]. Fundamentally interacting systems, such as Mott insulators like the $3d$ transition metal oxides (NiO [34], MnO [35], FeO, CeO [36]) or certain sulfides ($NiS_2$ [37]), are beyond the TQC classification scheme.

Here, we develop an interacting TQC (iTQC) formalism, which provides an extension of TQC that allows to also treat fundamentally interacting states [38]. To that end, we start by introducing a class of interacting reference states that extend the notion of ALs. Instead of the (single-particle) Bloch Hamiltonian and its "bands" in momentum space, we consider the $n$-particle Green's functions $g^{(n)}(\omega)$, with $\omega$ the Matsubara frequency, and we extend the concept of band representation to also be applicable in the context of these $n$-particle correlation functions. Specifically, we reinterpret the $n$-particle correlation functions as matrices in the space of $n$-particle excitations (hence, we denote them by an underscored symbol) and consider the correlation functions at zero frequency, where $\underline{g}^{(n)} \equiv \underline{g}^{(n)}(\omega = 0)$ are Hermitian, thereby admitting a spectral ordering. Correlation functions are well defined for interacting states, and they relate to experimental observables in some instances. They are also numerically accessible within advanced computational methods for modeling correlated quantum materials, such as quantum Monte Carlo (QMC) [39] and coupled cluster theory [40].

What type of topological phases can we expect to discover with this approach? First, as with TQC, the topological properties must be indicated or protected by spatial symmetries. Second, when working with $n$th-order Green's functions, the phases must be discoverable from $n$-body correlation functions. This is not the case for intrinsic topological order, as found in the fractional quantum Hall effect and various types of gapped spin liquids: discriminating these phases requires the measurement of correlation functions of extensive order $N$, where $N$ indicates the number of particles, that scales at least linearly with the system size [41].

In the presence of interactions, superconductivity and spontaneous symmetry breaking are abundant, and can be characterized by local-order parameters. However, featureless insulating phases, which are not adiabatically connected to free-fermion insulators, also exists and are known as symmetry-protected topological states (SPTs) [42]. These are presumably not as abundant and certainly very hard to discern and discover.

The reference states proposed later on in this paper are realizations of certain classes of "crystalline" and "point-group" SPTs (cSPTs and pgSPT, resp.) [43–47], in which a symmetry of the space group or point group acts as internal symmetry protecting the phase. Importantly, the reference states we propose capture a large set of cSPT classes, beyond the ones accessible through noninteracting states. Our formulation is suitable for identifying large classes of SPTs, naturally including all phases discoverable by TQC. Beyond TQC, there are fermionic SPT phases that are intrinsically interacting [48]. Our method is in particular susceptible to bosonic SPT phases of spins, which arise as effective descriptions of localized electrons and more broadly topological Mott insulators [49–52]. In the following, we focus on the "Hubbard" class of models for Mott insulators as one well-known example where such states arise. However, we expect our approach to be general enough to be extended beyond this class of models.

## II. SUMMARY OF RESULTS

The iTQC framework, summarized in Fig. 1, closely follows the basic ideas of TQC, which is the classification of ALs. An AL consists of atomic orbitals placed at lattice sites corresponding to some Wyckoff positions of the lattice. We first define a reference class of many-body states in Sec. III, which we dub $n$-Mott atomic limits ($n$-MALs), which consist of entangled clusters of $n$ electrons placed at some Wyckoff positions of the lattice. These entangled clusters can be constructed in such a way as to satisfy TRS as well as the lattice symmetries, but to transform nontrivially under the latter. More accurately, these reference states realize cSPTs connected to zero-dimensional (0D) block states, as discussed in Sec. III C. Note that, by contrast, to obtain a (noninteracting) AL state, which satisfies TRS, we must always combine Kramers pairs of orbitals at the same site, which transform trivially under any spatial symmetry. These ideas are summarized in Figs. 1(a)–1(c) for the case $n = 2$.

We use Green's functions as our main tool for diagnosing 2-MALs (see Sec. IV). While the single-particle Green's function is related to the Bloch Hamiltonian for a noninteracting system and thus, TQC can also be viewed as a classification scheme based on the single-particle Green's function, a many-body state is not fully specified by its single-particle Green's function. Consequently, we turn to the two-particle Green's function $\underline{g}^{(2)}$, for which we derive a crucial property: For an AL state, there is a lower bound on the eigenvalues of $\underline{g}^{(2)}$, which is given by the two-particle gap. Therefore, any eigenvalue of $\underline{g}^{(2)}$, which appears below this bound, originates from an interacting ground state. Our classification scheme thus focuses on this part of the spectrum of $\underline{g}^{(2)}$. Figures 1(d)–1(f) show a comparison of the classification based on TQC and iTQC.

The iTQC framework then allows to classify all the possible band representations of a $\underline{g}^{(n)}$ Green's function induced by $n$-MAL ground states as discussed in Sec. V. It is advantageous to consider an idealized limit, where the many-body Hamiltonian is spectrally flattened, in analogy with the band flattening procedure in the single-particle case. In this limit, we can derive analytical results for the $\underline{g}^{(2)}$ band structure. In particular, for an AL state, $\underline{g}^{(2)}$ only contains eigenvalues above the aforementioned bound [Fig. 1(e)]. However, for a 2-MAL state constructed as a product state of a single cluster operator acting on each unit cell, $\underline{g}^{(2)}$ contains a single eigenvalue below the bound, at each value of the momentum, whose eigenvector corresponds to the 2-MAL cluster operator out of which the 2-MAL state is formed [Fig. 1(g)]. We show that stacking several 2-MAL operators in each unit cell just leads to a direct sum of the $\underline{g}^{(2)}$ bands below the bound. If we consider all the possible 2-MAL operators compatible with a given space group and the $\underline{g}^{(2)}$ band structures induced by them, then we can check whether a given $\underline{g}^{(2)}$ band structure can be constructed out of a sum of 2-MAL band structures. Thus, iTQC provides a new definition of topological states: *If the band representation associated with the interaction-driven*

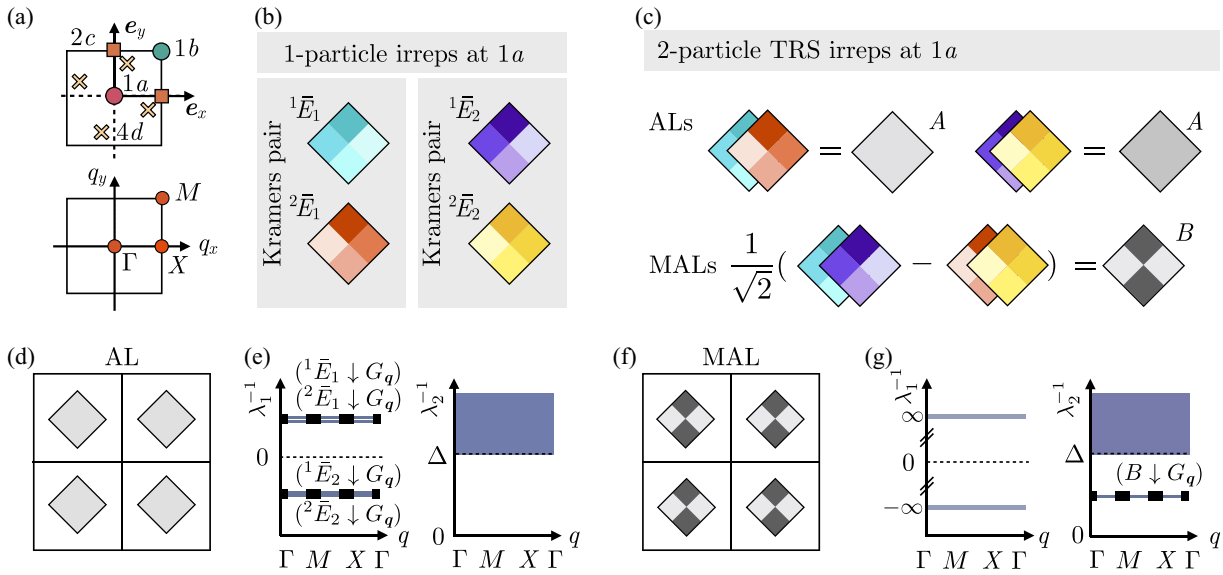


FIG. 1. Mott atomic limits and induced bands representations. (a) Unit cell and first Brillouin zone of the square lattice with the Wyckoff positions and high-symmetry points marked, respectively. (b) Two sets of single-particle irreps compatible with the site symmetry group $C_4^D$ of Wyckoff position $1a$ : The two blocks represent each two TRS-related states (Kramers pairs) and the colors indicate nontrivial rotation eigenvalues under $C_4$. (c) Examples of time-reversal symmetric two-particle irreps constructed out of the single-particle irreps in (b). In the first row we show two example of ALs: in this case, the two states of a Kramers pair from a Slater determinant and consequently, the state transforms in the $A$ representation of the point group. In the second row, we show an example of an MAL, where the state transforms in the $B$ representation of the point group. [(d),(f)] Show examples of two-particle irreps placed in each unit cell at Wyckoff position $1a$ with (d) an AL and (f) an MAL state on the square lattice. [(e),(g)] Schematically show the respective inverse spectra of the single-particle and two-particle Green's functions, marked by $\lambda_1^{-1}$ and $\lambda_2^{-1}$.

*spectrum of a Green's function cannot be induced from ALs and 2-MALs, the state is either (i) an SPT that cannot be induced from 0-dimensional blocks or (ii) it is a many-body state that is dominated by many-body correlations that involve more than two electrons.*

This statement represents an extension of the TQC framework that in principle can be naturally applied to $n \geqslant 2$.

For concreteness, we discuss the full classification of 2-MALs in one dimension (1D) (Sec. V C), which gives an explicit example of the procedure outlined above. In addition, simple two-dimensional (2D) examples where the classification can be done by hand are discussed in the Supplemental Material (SM) [55]. Finally, we apply our formalism in Sec. VI to four illustrative models whose ground states depart from ideal AL and 2-MAL states: (i) the Hubbard square [53], (ii) the Hubbard diamond chain [54], (iii) the Hubbard checkerboard lattice [53], and (iv) the Hubbard model on a star of David. In each case, we use exact diagonalization or QMC to diagnose AL and 2-MAL states, and the transitions between them.

In this paper, we restrict ourselves to the discussion of $n = 1$ and $n = 2$, while the explicit treatment of higher values of $n$ is left to future work. In addition, the ideas developed here are in principle easily extended to different types of $n$-particle correlation functions, alongside an appropriate class of reference states, while in the following we concentrate on the anomalous retarded particle-particle Green's function, for $n = 2$.

Further details can be found in the SM [55] (see also Refs. [56–59] therein).

## III. MOTT ATOMIC LIMITS

### A. *n*-MALs

As the overarching motivation of this paper is to develop a framework useful for making predictions about real crystalline materials, we focus on the case of TRS systems of itinerant electrons with spin-orbit coupling. We consider systems at zero temperature, gapped, short-range entangled, and with a unique ground state. This class of systems, encompassed by the SPT phases, has proven to be a promising domain for studying topological phenomena, and allows for a detailed characterization by first principles calculations. We will not consider any sublattice or chiral symmetry, as these are generically absent in real crystals.

With these constraints, we single out a class of interacting many-body states that our formalism is able to capture and classify, and that we consider as reference states of the SPT type. These states are the natural extension of the concept of ALs: while ALs are product states of exponentially localized single-particle states distributed on the lattice, $n$-MALs are product states of interacting clusters of $n$-electrons placed on the crystal.

To set the notation, we consider a lattice with space group $G$ with exponentially localized Wannier orbitals placed at some Wyckoff positions of the lattice. We denote by $\boldsymbol{x}_a$ the positions of the sites in the orbit of a Wyckoff position of multiplicity $m$, where $a = 1, \ldots, m$. The set of Wannier orbitals placed on the site at $\boldsymbol{x}_a$ must transform under a representation $\rho$ of its site-symmetry group $G_{\boldsymbol{x}_a}$.

With these notions, we define $\hat{c}^\dagger_{\boldsymbol{r},\alpha}$ ($\hat{c}_{\boldsymbol{r},\alpha}$) as the creation (annihilation) operator of an electron placed at the unit cell $\boldsymbol{r}$ and created (annihilated) in the single-particle state of an orbital whose quantum numbers are described by the compactified index $\alpha = (W, a, \rho, i)$. For an orbital located at $\boldsymbol{x}_a$, $W$ indicates the label of the Wyckoff position of the site at $\boldsymbol{x}_a$, $a = 1, \ldots, m$ specifies at which $\boldsymbol{x}_a$ the electron is placed, $\rho$ labels the representation of $G_{\boldsymbol{x}_a}$ of the orbital, and $i = 1, \cdots, \dim(\rho)$ enumerates the various orbitals placed at $\boldsymbol{x}_a$.

Noninteracting ALs are constructed as Slater determinants of exponentially localized single-electron states $\hat{c}_{\boldsymbol{r},\alpha}$, viz.,

$$|\mathrm{AL}\rangle = \prod_{\boldsymbol{r}} \prod_{\alpha \in \mathrm{occ.}} \hat{c}^\dagger_{\boldsymbol{r},\alpha} |0\rangle, \tag{1}$$

with $\alpha$ ranging over the occupied orbitals in each unit cell. In some instances, we may refer to $n$-ALs as states of the form (1) where each creation operator in (1) is replaced by a product of $n$ creation operators with different quantum numbers. A state is called *topological* if it is not possible to define exponentially localized Wannier orbitals compatible with the space group, such that the decomposition (1) holds. An elementary example are Chern bands in 2D. Therefore, in TQC, nontrivial topology refers to an obstruction in going from a filled band description in momentum space to a real space description in terms of localized orbitals.

We now introduce $n$-MALs, which are quantum many-body states of several electrons that are also exponentially localized, but may not be adiabatically connected to a single Slater determinant, or single reference state in quantum chemistry terms, without the breaking of a relevant spatial symmetry. The $n$-MALs are obtained by placing localized interacting clusters of electrons on (maximal) Wyckoff positions of the crystalline lattice, in analogy with the construction of ALs. Hence, the wave function of an $n$-MAL is

$$|n\text{-MAL}\rangle = \prod_{\boldsymbol{r}} \prod_{\xi \in \mathrm{occ.}} \hat{O}^\dagger_{\boldsymbol{r},\xi} |0\rangle, \tag{2}$$

where each $\hat{O}^\dagger_{\boldsymbol{r},\xi}$ is now a $n$-particle "cluster" operator, consisting of linear combinations of products of $n$ single-particle operators creating electrons centered at the unit cell with lattice vector $\boldsymbol{r}$, and the index $\xi$ ranges over the $n$-particle operators that are occupied in the unit cell.

To get an insight on the fundamental distinctions between ALs and $n$-MALs, note that TRS constrains all $n$-MALs to transform as real-valued 1D irreps of the site-symmetry group of their site, leaving $\pm 1$ as possible eigenvalues for any spatial symmetry. Conversely, TRS single Slater determinant states always transform with eigenvalue $+1$: They are composed of products of Kramers pairs of electrons, which contribute complex conjugate eigenvalues $\lambda$ and $\lambda^\star$, such that $\lambda\lambda^\star = +1$ is the symmetry eigenvalue of the whole pair [53]. Hence, $n$-MALs of type (2) are characterized by transformation rules under symmetry action that in principle can be distinct from the set of all the possible representation realized by TRS ALs.

Some of the states described by (2) can be adiabatically connected to ALs, while others form an adiabatically disconnected class of states. With the iTQC framework, we aim to identify these classes by means of the Green's function band representation, as we will discuss later.

Some prominent examples of $n$-MALs are (i) valence bond states [60], (ii) coupled cluster wave functions [40], and (iii) cluster Mott insulators with star of David order, as shown in this paper.

### B. 2-MALs

In practice, in the present paper we will specialize to the case $n = 2$. In the following, we denote 2-MALs as MALs for compactness of notation, unless otherwise stated, and maintain the label $n$-MALs for the general case.

A MAL can be in general written as

$$|\mathrm{MAL}\rangle = \prod_{\boldsymbol{r},\xi} \hat{O}^\dagger_{\boldsymbol{r},\xi} |0\rangle, \;\; \hat{O}^\dagger_{\boldsymbol{r},\xi} = \sum_{\alpha,\beta,\boldsymbol{u}} M^{\xi}_{\alpha\beta\boldsymbol{u}} \hat{c}^\dagger_{\boldsymbol{r},\alpha} \hat{c}^\dagger_{\boldsymbol{r}+\boldsymbol{u},\beta}, \tag{3}$$

where the coefficients $M^{\xi}_{\alpha\beta\boldsymbol{u}}$ are constrained by TRS and the spatial crystalline symmetries of the relevant space group, and $\xi$ labels the type of MAL cluster operator. We assume that distinct cluster operators do not overlap, and therefore $\hat{O}^\dagger_{\boldsymbol{r},\xi}$ commute pairwise [61], [62]. In Eq. (3), we introduce the lattice vector $\boldsymbol{u}$ to take into account the spatial separation between pairs of electrons. In momentum space, the MAL operator depends on a single momentum $\boldsymbol{q}$, and reads

$$\begin{aligned} \hat{O}^\dagger_{\boldsymbol{q},\xi} &= \frac{1}{\sqrt{N}} \sum_{\boldsymbol{r}} e^{-\mathrm{i}\boldsymbol{q}\cdot\boldsymbol{r}} \hat{O}^\dagger_{\boldsymbol{r},\xi} \\ &= \frac{1}{\sqrt{N}} \sum_{\boldsymbol{k},\alpha,\beta,\boldsymbol{u}} e^{\mathrm{i}(-\boldsymbol{k}+\boldsymbol{q})\cdot\boldsymbol{u}} M^{\xi}_{\alpha\beta\boldsymbol{u}} \hat{c}^\dagger_{\boldsymbol{k},\alpha} \hat{c}^\dagger_{-\boldsymbol{k}+\boldsymbol{q},\beta}. \end{aligned} \tag{4}$$

Note that the definition in Eq. (3) also includes ALs with an even number of electrons. The MAL operators transform under two-particle representations $\rho$ of the space group $G$. We discuss the explicit form of $\rho$ and how to systematically construct MAL operators compatible with a certain space group $G$ in the SM [55].

As an explicit example of MALs, we consider a 1D lattice. Depending on the spatial embedding in a 3D system, the 1D system may be considered in the presence of mirror symmetry or inversion symmetry ($\mathcal{I}$) [63], and in the following we only focus on the latter. Let us consider the case of Wyckoff position $2c$, which has twofold multiplicity, equipped with a Kramers pair of orbitals (Fig. 4). We denote the creation operator at the unit cell coordinate $r = 0, \cdots L-1$ as $\hat{c}^\dagger_{r,a,\sigma}$, where $\sigma \in \{\uparrow, \downarrow\}$ is the spin, and $a \in \{1, 2\}$ labels the two $2c$ sites [64]. The antiunitary TRS acts as

$$\mathcal{T} \hat{c}^\dagger_{r,a,\sigma} \mathcal{T}^{-1} = \mathrm{i} \sum_{\sigma'=\uparrow,\downarrow} \sigma^{(2)}_{\sigma'\sigma} \hat{c}^\dagger_{r,a,\sigma'}, \tag{5}$$

where we denote with $\sigma^{(i)}$, $i = 1, 2, 3$ the three Pauli matrices, and inversion acts as

$$\mathcal{I} \hat{c}^\dagger_{r,a,\sigma} \mathcal{I}^{-1} = \sum_{a'=1,2} \sigma^{(1)}_{a'a} \hat{c}^\dagger_{-r,a',\sigma}, \tag{6}$$

where we understand $r \mod L$. An example of a two-electron cluster operator, constructed out of the available single-electron creation operators, is

$$\hat{O}^\dagger_{r,\mathrm{MAL}} = \frac{1}{\sqrt{2}} (\hat{c}^\dagger_{r,1,\uparrow} \hat{c}^\dagger_{r,1,\downarrow} - \hat{c}^\dagger_{r,2,\uparrow} \hat{c}^\dagger_{r,2,\downarrow}), \tag{7}$$

which obeys

$$\mathcal{I}\hat{O}^{\dagger}_{r,\mathrm{MAL}}\mathcal{I}^{-1} = -\hat{O}^{\dagger}_{-r,\mathrm{MAL}}. \tag{8}$$

The operator in Eq. (8) creates a two-electron cluster that transforms with inversion eigenvalue $(-1)$, when we choose $r = 0$ as inversion center. It is easy to prove that the ground state

$$|\mathrm{MAL}\rangle = \prod_{r=0}^{L-1} \hat{O}^{\dagger}_{r,\mathrm{MAL}}|0\rangle \tag{9}$$

cannot be connected adiabatically to any 2-AL ground state: For odd $L$, it has inversion eigenvalue $(-1)$, while any TRS AL state has inversion eigenvalue $(+1)$ [53]. As no TRS AL behaves the same way at the same filling, the state in Eq. (9) has to be considered as a representative of a distinct phase.

### C. MALs and SPTs

We now discuss how MALs realize SPT phases. Crystalline SPTs and pgSPTs [43–47] are SPT phases whose protecting symmetries are crystalline space-group or point-group symmetries, which act as internal on-site operations on portions of the unit cell, called "blocks" in this context [65]. A block $b$ of the unit cell is left invariant under a subset of the point group, $G_b \subset G$, i.e., elements of $G_b$ act as on-site or internal symmetries on the block. Let us first recall a few properties of the pgSPTs, following Ref. [43]. A possible construction scheme for such phases consists in decorating different $d_b$-dimensional unit cell blocks $b$ ($d_b = 0, 1, 2$ for 3D systems) with $d_b$-dimensional SPTs. In Ref. [43], Eq. (1) defines the "block states" as

$$|\Psi\rangle = \bigotimes_{b\in B} |\psi_b\rangle\,, \tag{10}$$

where each factor $|\psi_b\rangle$ corresponds to an SPT wavefunction in $d_b$ dimensions defined on block $b$, whose protecting symmetry belongs to $G_b$. For the case of a 0D block, one says that $|\psi_b\rangle$ has a "$G_b$ charge", meaning that it transforms under a 1D $G_b$ irrep, and different irreps correspond to distinguished 0D-block SPTs. The classifications of pgSPTs with point group $G$ in $d$ dimensions and bosonic degrees of freedom are provided by the cobordism classification, and can be decomposed as follows (Eq. 2 in Ref. [43])

$$\mathcal{C}(G) = \mathcal{C}_0(G) \times \cdots \times \mathcal{C}_{d-1}(G), \tag{11}$$

where $\mathcal{C}_{d_b}(G)$ is the classification of SPTs built only out of $d_b$ blocks. For fermionic degree of freedom the factorization of Eq. (11) does not hold, a fact that we can ignore in this paper, as we argue below.

From Eqs. (3) and (10), we see that MALs are 0D-block state cSPTs. Our interest here are TRS fermionic MALs that conserve particle number. Particle number conservation $U(1)$ and TRS $\mathcal{T}$ thus have to be imposed in addition to the symmetry $G$. MALs have even fermion parity, otherwise they would not have a unique TRS ground state. Therefore, time-reversal $\mathcal{T}^2 = (-1)^F = +1$ ($F$ being the fermion parity) is represented as in bosonic states. MALs thus follow the bosonic $\mathcal{C}_0(G)$ classification, supplemented by the TRS constraint and particle number conservation. The relevant symmetry group

TABLE I. Classification of 0D-block SPTs. Classification of SPT phases constructed from 0D-block states, where the symmetries of the systems include charge conservation $U(1)$, and TRS $\mathbb{Z}_4^{TF}$, generated by $\mathcal{T} = T\mathcal{K}$, where $T$ is the unitary part of TRS and $\mathcal{T}^2 = (-1)^F$, $F$ the fermion parity. The three columns correspond to the case of no additional internal symmetry (indicated by $\mathbb{Z}_1$), and a twofold graded internal symmetry that commutes (indicated by $\mathbb{Z}_2$, $[S,T] = 0$) or anticommutes (indicated by $\mathbb{Z}_2$, $\{S,T\} = 0$) with the unitary part of TRS.

| $\frac{U(1)\times\mathbb{Z}_4^{TF}}{\mathbb{Z}_2^F}$ | $\mathbb{Z}_1$ | $\mathbb{Z}_2$, $[S,T]=0$ | $\mathbb{Z}_2$, $\{S,T\}=0$ |
|---|---|---|---|
| Noninteracting | $\mathbb{Z}$ | $\mathbb{Z}\times\mathbb{Z}$ | $\mathbb{Z}$ |
| Interacting | $\mathbb{Z}$ | $\mathbb{Z}\times\mathbb{Z}\times\mathbb{Z}_2$ | $\mathbb{Z}\times\mathbb{Z}_2$ |

for classifying the 0D-block SPTs is thus $G_0 = \frac{U(1)\times\mathbb{Z}_4^{TF}}{\mathbb{Z}_2^F} \times \tilde{G}$, where $\tilde{G}$ is the unitary on-site symmetry of the block, and $\mathbb{Z}_2^F$ is the fermion partity. For concreteness, we exemplify this for the case $\tilde{G} = \mathbb{Z}_2$ with generator $S$ that could originate from mirror, twofold rotation or inversion symmetry and contrast it to $\tilde{G} = \mathbb{Z}_1$. Table I lists the classification for both cases, differentiating whether the system is interacting or not. The noninteracting case corresponds to ALs, where $\mathbb{Z}$ simply counts the number of occupied Kramers pairs. Importantly, interactions allow for an additional $\mathbb{Z}_2$ grading, which is realized by MALs and allows for 0D-block states odd under $S$. We illustrate in Fig. 2(a) how these blocks can be used to build pgSPTs in wallpaper group $p4$, that has fourfold rotation symmetry and translation symmetry. At the Wyckoff positions $1a$ and $1b$ we can place MALs with $C_4$ eigenvalues $\pm1$ and at the Wyckoff position $2c$ we can place MALs with $C_2$ eigenvalues $\pm1$. This results in a $\mathbb{Z}_2 \times \mathbb{Z}_2 \times \mathbb{Z}_2$ group of pgSPT phases beyond those that have an AL representation.

A practical question is, given a (non-fixed-point) correlated many-body state, how one computes topological invariants that allow to place the state in this classification. These SPT invariants can be obtained as the $U(1)$ phases of a quantum system defined on a spacetime manifold potentially equipped with a background symmetry bundle and having a topology, which probes the relevant spatial symmetries. Thus far, such invariants have been extracted from the ground states of interacting models for only a handful of examples by applying partial symmetry operations [66,67], by gauging the protecting symmetry [68], and by computing a partial transpose

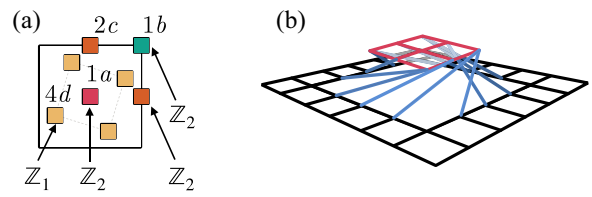


FIG. 2. Crystalline SPTs. (a) Classification of 0D-block cSPTs in a $C_4$ symmetric unit cell with TRS $\mathcal{T}^2 = +1$. (b) Illustration of the action of a partial symmetry operation applied to a subsystem in the square lattice. The pink region indicates the subsystem and the blue lines indicate the new lattice connections after the partial $C_4$ rotation is applied to the subsystem.

operation [69]. Concretely, the invariants are obtained as the ground-state expectation value of a partial point-group operation, i. e., a point-group operation applied to a subsystem. Since one needs to perform such an operation on a subregion of the space that is large compared with the correlation length of the system, it typically involves taking the expectation value of an operator that implements $\mathcal{O}(L^d)$ swap operations where $L > \xi$ (the correlation length) and $d$ is the dimension of space. Figure 2(c) shows an example of how a partial symmetry operation acts for the square lattice case: first, the $C_4$ rotation is applied to a subsystem of size $L^d$, comparable with the total system size, while leaving the rest of the system unchanged. The expectation value of this operation on the initial ground state allows to extract the topological invariant.

Depending on the form in which the state is represented, the computation of such an expectation value can be of vastly different numerical complexity. In 1D systems, if the ground state is known in a matrix-product state (MPS) form, it is possible to efficiently evaluate the partial symmetry action on the ground state [70]. On the other hand, diagrammatic QMC calculations as well as higher-dimensional tensor networks are typically not suited for computing such high-order operator expectation values.

## IV. GREEN'S FUNCTIONS

### A. Single-particle retarded Green's function

In this section, we review a few properties of the single-particle Green's functions, which will be relevant in connection to higher-order Green's functions.

Consider in real time the retarded Green's function with an electron created at time $t = 0$ and another annihilated at time $t$,

$$g^{(1)}_{\alpha\beta}(t, \boldsymbol{k}) = \mathrm{i}\Theta(t)\langle\{\hat{c}_{\boldsymbol{k},\alpha}(t), \hat{c}^\dagger_{\boldsymbol{k},\beta}(0)\}\rangle_{\mathrm{GS}}, \tag{12}$$

where the brackets $\langle ... \rangle_{\mathrm{GS}}$ indicate the expectation value over the ground state (assumed to be unique and gapped), and $\boldsymbol{k}, \alpha, \beta$ describe the quantum numbers of the created and annihilated electrons. Equivalently, we can write the single-particle Green's function in terms of Matsubara frequency $\omega$. Focusing on the case of zero frequency for reasons that will become clear in the following discussion, by Fourier transforming Eq. (12) to Matsubara frequency and setting $\omega = 0$ we obtain

$$\begin{aligned} g^{(1)}_{\alpha\beta}(\omega = 0, \boldsymbol{k}) = &- \langle\hat{c}_{\boldsymbol{k},\alpha}[\hat{H} - E_0]^{-1}\hat{c}^\dagger_{\boldsymbol{k},\beta}\rangle_{\mathrm{GS}} \\ &+ \langle\hat{c}^\dagger_{\boldsymbol{k},\beta}[\hat{H} - E_0]^{-1}\hat{c}_{\boldsymbol{k},\alpha}\rangle_{\mathrm{GS}} \end{aligned} \tag{13}$$

with $\hat{H}$ the many-body Hamiltonian of the system, and $E_0$ the energy of the ground state. Although Eq. (13) results in a single number, for a specific choice of $\{\boldsymbol{k}, \alpha, \beta\}$, the collection of all the possible $g^{(1)}_{\alpha\beta}(\omega = 0, \boldsymbol{k})$ can be interpreted as a matrix $\underline{g}^{(1)}(\omega = 0, \boldsymbol{k})$ with indices $\alpha, \beta$, for each sector of fixed $\boldsymbol{k}$—where here and in the following we use the underscore to denote matrices. This interpretation of the single-particle Green's function as a matrix allows to compute a spectrum of $\underline{g}^{(1)}(\omega = 0, \boldsymbol{k})$. Note that $\underline{g}^{(1)}(\omega = 0, \boldsymbol{k})$ is a hermitian matrix, yielding a real spectrum. The eigenstates $v^\xi$ of $\underline{g}^{(1)}(\omega = 0, \boldsymbol{k})$ naturally define operators of the type

$$\hat{a}^\dagger_{\boldsymbol{k},\xi} = \sum_\alpha v^\xi_\alpha \hat{c}^\dagger_{\boldsymbol{k},\alpha}, \tag{14}$$

which we refer to as the eigenstates of $\underline{g}^{(1)}(\omega = 0, \boldsymbol{k})$.

We first recall the role of $\underline{g}^{(1)}(\omega, \boldsymbol{k})$ for noninteracting systems. In this case, the Hamiltonian is written as

$$\hat{H} = \sum_{\boldsymbol{k},\alpha,\beta} \hat{c}^\dagger_{\boldsymbol{k},\alpha} h(\boldsymbol{k})_{\alpha\beta} \hat{c}_{\boldsymbol{k},\beta}, \tag{15}$$

and the single-particle Bloch Hamiltonian $h(\boldsymbol{k})$ is related to $\underline{g}^{(1)}(\omega, \boldsymbol{k})$ through the relation $\underline{g}^{(1)}(\omega, \boldsymbol{k}) = [\mathrm{i}\omega - h(\boldsymbol{k})]^{-1}$. Based on these considerations, TQC can be thought of as a classification scheme for the spectrum of $\underline{g}^{(1)}(\omega = 0, \boldsymbol{k})$ instead of the band representations of $h(\boldsymbol{k})$ [71]. [In the following, we refer to $\underline{g}^{(1)}(\omega = 0, \boldsymbol{k})$ as $\underline{g}^{(1)}(\boldsymbol{k})$ or simply $\underline{g}^{(1)}$, when we consider all the $\boldsymbol{k}$ sectors at once, as we always set the frequency to be equal to zero, unless otherwise stated.] The eigenvectors of $\underline{g}^{(1)}(\boldsymbol{k})$, as defined in Eq. (14), are thus the single-particle states, which make up the single Slater determinant ground state, and the eigenvalues yield the inverse energies. Also, states obtained by applying the operators (14) on the vacuum are eigenstates of the Hamiltonian. In fact, the spectrum of $-[\underline{g}^{(1)}]^{-1}$ can be interpreted as a band structure, and in this sense we speak about the "band representation" of $\underline{g}^{(1)}$. Turning to the case with interactions, one possible avenue to extend TQC is to calculate $\underline{g}^{(1)}(\omega = 0, \boldsymbol{k})$ and invert it to obtain an effective Hamiltonian. Indeed, previous works have focused on applying the TQC framework to the single-particle Green's function in the interacting case, and the resulting effective Hamiltonian was termed *topological Hamiltonian* [54,72–76], which also includes the self-energy. The choice of considering $\underline{g}^{(1)}$ at zero frequency relies on it being sufficient to capture the topological properties of the system. This approach has proven successful in capturing topological properties of states that are adiabatically connected to noninteracting systems (single Slater determinants). The only significant difference to classifying band structures of Bloch Hamiltonians regards the notion of equivalence classes via band gaps: For two band representations of $\underline{g}^{(1)}$ to be equivalent, they have to be deformable into each other (while retaining symmetries and the locality of the operator) not only without any eigenvalue crossing infinity (corresponding to the normal noninteracting band gap), but also with no eigenvalue crossing zero (corresponding to poles in the self-energy when Mott gaps open) [75,77].

However, unlike the noninteracting case, an interacting state is generically not fully specified by $\underline{g}^{(1)}$, and for intrinsically interacting topological states the aforementioned approach to identify topology fails. For interacting states, there are in general a number of nontrivial $n$-particle Green's functions $g^{(n)}$, where $n = 1, \cdots, N$ for a system with particle number $N$, which cannot be reconstructed from the sole knowledge of $\underline{g}^{(1)}$. While evaluating all the $N$ correlation functions is not feasible in practice, one can truncate the series, as is done in the Bogoliubov-Born-Green-Kirkwood-Yvon hierarchy [78]. For some classes of states, this truncation is exact: For instance, in the $n$-MALs states the $n$-particle Green's function completely describes the system, since correlations

are constrained to involve at most $n$ electrons at a time, if the $n$-particle operators creating clusters of electrons at different unit cells do not overlap. Based on this statement, we will see in Sec. V how to use $\underline{g}^{(2)}$ to diagnose the interacting or noninteracting nature and symmetry properties of an MAL ground state. In the present paper, we focus on the information contained in the two-particle Green's function $\underline{g}^{(2)}$, although in principle the generalization to higher-order Green's functions $\underline{g}^{(n)}$ should be straightforward.

### B. Two-particle retarded Green's function

We build the iTQC formalism based on the two-particle retarded Green's function describing the amplitude for the creation of two electrons at real time $t = 0$, and the annihilation of two electrons at a later time $t$,

$$g^{(2)}_{\boldsymbol{r}_1\boldsymbol{r}_2,\boldsymbol{r}'_2\boldsymbol{r}'_1;\alpha\beta,\gamma\delta}(t) = -\Theta(t)\left\langle\left[\hat{c}_{\boldsymbol{r}_2,\beta}(t)\hat{c}_{\boldsymbol{r}_1,\alpha}(t),\, \hat{c}^\dagger_{\boldsymbol{r}'_1,\gamma}(0)\hat{c}^\dagger_{\boldsymbol{r}'_2,\delta}(0)\right]\right\rangle_{\mathrm{GS}}. \tag{16}$$

Again, the expectation value $\langle\cdots\rangle_{\mathrm{GS}}$ is taken over the many-body ground state of the Hamiltonian. The transformed version of Eq. (16) as a function of imaginary (Matsubara) frequency $\omega$ reads

$$g^{(2)}_{\boldsymbol{r}_1\boldsymbol{r}_2,\boldsymbol{r}'_2\boldsymbol{r}'_1;\alpha\beta,\gamma\delta}(\omega) = -\left\langle\hat{c}_{\boldsymbol{r}_2,\beta}\hat{c}_{\boldsymbol{r}_1,\alpha}[\mathrm{i}\omega + E_0 - \hat{H}]^{-1}\hat{c}^\dagger_{\boldsymbol{r}'_1,\gamma}\hat{c}^\dagger_{\boldsymbol{r}'_2,\delta}\right\rangle_{\mathrm{GS}} + \left\langle\hat{c}^\dagger_{\boldsymbol{r}'_1,\gamma}\hat{c}^\dagger_{\boldsymbol{r}'_2,\delta}[\mathrm{i}\omega - E_0 + \hat{H}]^{-1}\hat{c}_{\boldsymbol{r}_2,\beta}\hat{c}_{\boldsymbol{r}_1,\alpha}\right\rangle_{\mathrm{GS}}, \tag{17}$$

where $E_0$ indicates the ground state energy and $\hat{H}$ is the many-body Hamiltonian of the system. It is useful to write Eq. (17) in the Lehmann decomposition [79],

$$g^{(2)}_{\boldsymbol{r}_1\boldsymbol{r}_2,\boldsymbol{r}'_2\boldsymbol{r}'_1;\alpha\beta,\gamma\delta}(\omega) = -\sum_{m\in\mathscr{H}_{N+2}}\frac{\langle\mathrm{GS}|\,\hat{c}_{\boldsymbol{r}_2,\beta}\hat{c}_{\boldsymbol{r}_1,\alpha}\,|m\rangle\,\langle m|\,\hat{c}^\dagger_{\boldsymbol{r}'_1,\gamma}\hat{c}^\dagger_{\boldsymbol{r}'_2,\delta}\,|\mathrm{GS}\rangle}{\mathrm{i}\omega + E_0 - E_m} + \sum_{n\in\mathscr{H}_{N-2}}\frac{\langle\mathrm{GS}|\,\hat{c}^\dagger_{\boldsymbol{r}'_1,\gamma}\hat{c}^\dagger_{\boldsymbol{r}'_2,\delta}\,|n\rangle\,\langle n|\,\hat{c}_{\boldsymbol{r}_2,\beta}\hat{c}_{\boldsymbol{r}_1,\alpha}\,|\mathrm{GS}\rangle}{\mathrm{i}\omega - E_0 + E_n}, \tag{18}$$

where $\mathscr{H}_{N\pm2}$ indicates the Hilbert space of $N \pm 2$ particles, and we assumed that the many-body ground state lies in the $N$-particle sector of the Fock space. Expressions analogous to Eqs. (16), (17), and (18) apply for electronic creation and annihilation operators acting in momentum space. The counterpart of (17) with electronic operators acting in momentum space is

$$g^{(2)}_{\boldsymbol{k}_1,\boldsymbol{k}_2,\alpha\beta,\gamma\delta}(\omega,\boldsymbol{q}) = -\left\langle\hat{c}_{-\boldsymbol{k}_1+\boldsymbol{q},\beta}\hat{c}_{\boldsymbol{k}_1,\alpha}[\mathrm{i}\omega + E_0 - \hat{H}]^{-1}\hat{c}^\dagger_{\boldsymbol{k}_2,\gamma}\hat{c}^\dagger_{-\boldsymbol{k}_2+\boldsymbol{q},\delta}\right\rangle_{\mathrm{GS}} + \left\langle\hat{c}^\dagger_{\boldsymbol{k}_2,\gamma}\hat{c}^\dagger_{-\boldsymbol{k}_2+\boldsymbol{q},\delta}[\mathrm{i}\omega - E_0 + \hat{H}]^{-1}\hat{c}_{-\boldsymbol{k}_1+\boldsymbol{q},\beta}\hat{c}_{\boldsymbol{k}_1,\alpha}\right\rangle_{\mathrm{GS}}, \tag{19}$$

which is determined by three different momenta: the internal momenta $\boldsymbol{k}_1$, $\boldsymbol{k}_2$, and the total momentum exchanged $\boldsymbol{q}$. We now restrict our attention to a smaller class of Green's functions, as compared to Eq. (19), by introducing the constraint that the pair of operators that create (annihilate) electrons are local in space. The requirement of locality is obtained by demanding that they are not further than a certain distance $u_{\max}$ apart, meaning $\boldsymbol{r}_2 = \boldsymbol{r}_1 + \boldsymbol{u}$ and $\boldsymbol{r}'_2 = \boldsymbol{r}'_1 + \boldsymbol{v}$, for a range of $|\boldsymbol{u}|, |\boldsymbol{v}| < u_{\max}$. This allows to include correlations between pairs of electrons on sufficiently short distances, which we expect to be the ones dominating the essential entanglement structure of a gapped ground state. Note that $\boldsymbol{u}$, $\boldsymbol{v}$ also depend on the indices $\alpha$, $\gamma$, and in principle also condition the allowed $\beta$, $\delta$ (see the SM [55]). This constraint of locality is necessary to obtain a finite dimensional matrix from the set of $g^{(2)}$ expectation values, such that its dimensions are independent of system size—at fixed $\boldsymbol{q}$. The more generic type of $g^{(2)}$, as the one in Eq. (19), has the momentum labels $\boldsymbol{k}_1, \boldsymbol{k}_2$, apart from $\boldsymbol{q}$, over which it needs to be diagonalized, leading to a number of eigenvalues that does not increase linearly with system size.

With the locality constraint in place and by taking into account translational invariance, one obtains

$$\begin{aligned} g^{(2)}_{\alpha\beta\boldsymbol{u},\gamma\delta\boldsymbol{v}}(\omega,\boldsymbol{q}) &= \frac{1}{N}\sum_{\boldsymbol{r},\boldsymbol{r}'} e^{\mathrm{i}\boldsymbol{q}\cdot(\boldsymbol{r}-\boldsymbol{r}')} g^{(2)}_{\boldsymbol{r},\boldsymbol{r}+\boldsymbol{u},\boldsymbol{r}',\boldsymbol{r}'+\boldsymbol{v},\alpha\beta,\gamma\delta}(\omega) \\ &:= \frac{1}{N}\sum_{\boldsymbol{r},\boldsymbol{r}'} e^{\mathrm{i}\boldsymbol{q}\cdot(\boldsymbol{r}-\boldsymbol{r}')} g^{(2)}_{\boldsymbol{r},\boldsymbol{r}',\alpha\beta\boldsymbol{u},\gamma\delta\boldsymbol{v}}(\omega) \\ &= \frac{1}{N}\sum_{\boldsymbol{k}_1,\boldsymbol{k}_2} e^{\mathrm{i}(-\boldsymbol{k}_1+\boldsymbol{q})\cdot\boldsymbol{u}} e^{-\mathrm{i}(-\boldsymbol{k}_2+\boldsymbol{q})\cdot\boldsymbol{v}} g^{(2)}_{\boldsymbol{k}_1,\boldsymbol{k}_2,\alpha\beta,\gamma\delta}(\omega,\boldsymbol{q}), \end{aligned} \tag{20}$$

showing that our requirement of locality is in fact equivalent to tracing out the internal momenta $\boldsymbol{k}_1$ and $\boldsymbol{k}_2$.

In analogy to the discussion in Sec. IV A, the collection of all the expectation values (20) can be recast into a matrix, indicated as $\underline{g}^{(2)}(\omega,\boldsymbol{q})$. For each value of momentum $\boldsymbol{q}$, we define $\{(\alpha,\beta,\boldsymbol{u}),(\gamma,\delta,\boldsymbol{v})\}$ as compact indices for $\underline{g}^{(2)}(\omega,\boldsymbol{q})$. This corresponds to considering the two electronic creation (annihilation) operators as a single operator, and the Green's function can be seen as a matrix with entries

$$g^{(2)}_{(\alpha\beta\boldsymbol{u}),(\gamma\delta\boldsymbol{v})}(\omega=0,\boldsymbol{q}) = \langle\hat{O}_{\boldsymbol{q},(\alpha\beta\boldsymbol{u})}[\hat{H}-E_0]^{-1}\hat{O}^\dagger_{\boldsymbol{q},(\gamma\delta\boldsymbol{v})}\rangle_{\mathrm{GS}} + \langle\hat{O}^\dagger_{\boldsymbol{q},(\gamma\delta\boldsymbol{v})}[\hat{H}-E_0]^{-1}\hat{O}_{\boldsymbol{q},(\alpha\beta\boldsymbol{u})}\rangle_{\mathrm{GS}}, \tag{21}$$

where we defined

$$\hat{O}^\dagger_{\boldsymbol{q},(\gamma\delta\boldsymbol{v})} = \frac{1}{\sqrt{N}}\sum_{\boldsymbol{k}} e^{\mathrm{i}(-\boldsymbol{k}+\boldsymbol{q})\cdot\boldsymbol{v}}\hat{c}^\dagger_{\boldsymbol{k},\gamma}\hat{c}^\dagger_{-\boldsymbol{k}+\boldsymbol{q},\delta}. \tag{22}$$

We dub the matrix $\underline{g}^{(2)}(\omega=0,\boldsymbol{q})$ with entries defined in Eq. (21) the *two-particle radius confined Green's function*, which is the central object for the classification of MAL states presented in this work. In the following, we refer to $\underline{g}^{(2)}(\omega=0,\boldsymbol{q})$ as $\underline{g}^{(2)}(\boldsymbol{q})$—or simply $\underline{g}^{(2)}$ when all the $\boldsymbol{q}$ sectors are considered—for compactness. We note that for bosonic correlation functions, there can be an order-of-limits ambiguity with respect to taking the limits $\omega \to 0$ and $\boldsymbol{q} \to 0$. In our computations we always perform the $\omega \to 0$ limit first by setting $\omega = 0$ from the start. Since Eq. (21) depends on a single momentum $\boldsymbol{q}$, the number of its eigenvalues scales linearly with the system size. Hence, by diagonalizing the

matrix $\underline{g}^{(2)}(\boldsymbol{q})$ at each $\boldsymbol{q}$, one obtains a set of eigenvalues that can be interpreted as a "band structure" of $\underline{g}^{(2)}$. Each eigenstate $v^{\xi}_{\boldsymbol{q}(\alpha\beta\boldsymbol{u})}$ of the matrix $\underline{g}^{(2)}$ can now naturally be used to define a two-particle operator

$$\hat{O}^{\dagger}_{\boldsymbol{q},\xi} = \frac{1}{\sqrt{N}} \sum_{(\alpha\beta\boldsymbol{u})} v^{\xi}_{\boldsymbol{q}(\alpha\beta\boldsymbol{u})} \sum_{\boldsymbol{k}} e^{\mathrm{i}(-\boldsymbol{k}+\boldsymbol{q})\cdot\boldsymbol{u}} \hat{c}^{\dagger}_{\boldsymbol{k},\alpha} \hat{c}^{\dagger}_{-\boldsymbol{k}+\boldsymbol{q},\beta}, \tag{23}$$

which we will refer to as an eigenstate of $\underline{g}^{(2)}$. After diagonalizing $\underline{g}^{(2)}$, we consider its inverse spectrum rather than the original set of eigenvalues, in analogy to the approach used to analyze $\underline{g}^{(1)}$ and such that the resulting eigenvalues can be expressed in units of energy.

Note that, when the ground state is a noninteracting state (hence a single Slater determinant) and at $\omega = 0$, for any eigenvalue $\lambda_2$ of $\underline{g}^{(2)}$ it holds that

$$\frac{1}{\lambda_2} \geqslant \Delta_{\underline{g}^{(2)}} := \min(\Delta_{N+2},\ \Delta_{N-2}), \tag{24}$$

where we defined

$$\begin{aligned} \Delta_{N+2} &:= E_{\min}(N+2) - E_0 > 0, \\ \Delta_{N-2} &:= E_{\min}(N-2) - E_0 > 0, \end{aligned} \tag{25}$$

with $E_{\min}(N \pm 2)$ the lowest energy eigenvalue of the Hamiltonian in the $N \pm 2$ particle sector. The latter statement can be understood by considering the electronic operators in Eq. (23) in the diagonal basis of the noninteracting Hamiltonian $\hat{H}$. Each eigenstate of $\underline{g}^{(2)}$ can lead to a nonzero expectation value for one and only one of the two terms in Eq. (18), while the other one has to give a zero contribution. When both the single-particle operators appearing in the two-particle eigenstates correspond to nonoccupied states in the noninteracting ground state, they contribute to the first term in Eq. (21), while if they are both occupied they only contribute to the second term in Eq. (21). For a two-particle operator with one occupied and one nonoccupied operator, the total contribution is zero. Therefore, any eigenvalue of $\underline{g}^{(2)}$ that violates the bound (24) is an indication of an interacting ground state, since it would not be present in a purely Slater determinant state. These are the eigenvalues that we focus on in our classification scheme.

The eigenvalues of $\underline{g}^{(1)}$ and $\underline{g}^{(2)}$ taken at zero frequency do not have an immediate physical interpretation in terms of quasiparticles [74], but nevertheless some understanding in this direction can be developed. An eigenstate $\hat{O}^{\dagger}_{\boldsymbol{q},\xi}$ of the two-particle Green's function naturally corresponds to two-particle excited states of the form

$$|\Psi_{\mathrm{ex}}\rangle = \hat{O}^{\dagger}_{\boldsymbol{q},\xi} |\mathrm{GS}\rangle\,, \quad |\bar{\Psi}_{\mathrm{ex}}\rangle = \hat{O}_{\boldsymbol{q},\xi} |\mathrm{GS}\rangle\,, \tag{26}$$

with $\hat{O}^{\dagger}_{\boldsymbol{q},\xi}$ as defined in Eq. (23). In the case of a generic state, Eq. (26) will not give exact eigenstates of the Hamiltonian; however, they can serve as an ansatz for two-particle excitations. The $[\underline{g}^{(2)}]^{-1}$ eigenvalue with eigenstate $\hat{O}^{\dagger}_{\boldsymbol{q},\xi}$ gives an estimate of the energy difference between the particle-particle ($|\Psi_{\mathrm{ex}}\rangle$) and hole-hole ($|\bar{\Psi}_{\mathrm{ex}}\rangle$) excited states. Therefore, states of the form Eq. (26) corresponding to eigenstates violating the bound (24) can be interpreted as "bound states" in the particle-particle spectra. States that are far above the bound (24) will correspond to the particle-particle continuum and are therefore less interesting. For the systems we study, the particle-particle continuum is generally well separated from the bound states below the bound, allowing these eigenstates to be clearly identified. For systems where this separation of scales is not clear, our method will not be applicable.

Let us finally comment on the choice of Green's function. Whereas an AL is created by acting with one-particle electron operators, Eq. (1), a 2-MAL is created by acting on the vacuum with a two-particle operator, Eq. (2). The noninteracting topology is successfully diagnosed with the Green's function of Eq. (13) and this motivates the choice of Eq. (21), i. e., the particle-particle response function, to diagnose the topology of interacting states, as it resembles the structure of the single-particle correlation function, with the replacement of single-particle operators with two-particle operators. Indeed, as discussed in the later sections, this quantity shows a clear and easily identifiable signature of a MAL phase in terms of a single low-lying band.

However, this choice of two-particle correlation function is not the only possibility. Instead of considering the Green's function of the form of Eq. (20), we could for instance evaluate the Green's function of the particle-hole type, i. e.,

$$\begin{aligned} &g^{(2)}_{\mathrm{ph},\boldsymbol{r}_1,\boldsymbol{r}_2,\boldsymbol{r}'_1,\boldsymbol{r}'_2,\alpha,\beta,\gamma,\delta}(\omega) \\ &\quad = \mathrm{FT}_{\omega}\big[ -\Theta(t)\big\langle\big[\hat{c}^{\dagger}_{\boldsymbol{r}_2,\beta}(t)\hat{c}_{\boldsymbol{r}_1,\alpha}(t),\, \hat{c}^{\dagger}_{\boldsymbol{r}'_1,\gamma}(0)\hat{c}_{\boldsymbol{r}'_2,\delta}(0)\big]\big\rangle\big], \end{aligned} \tag{27}$$

which probes particle-hole like excitations on the ground state, as opposed to particle-particle excitations. This correlation function, rearranged into a matrix and after setting $\omega = 0$, has a positive semidefinite spectrum, and it has a noninteracting bound analogous to the one of Eq. (24). In this case, the bound is set by $1/\Delta_N$, where $\Delta_N = E_{\mathrm{ex}}(N) - E_0$ is the energy gap in the $N$-particle sector, with $E_{\mathrm{ex}}(N)$ the energy of the first excited state in the $N$-particle sector. This is true if one discards the contribution coming from the overlap with the ground state in the Lehmann decomposition, which would result into a divergent eigenvalue. Although the particle-hole Green's function may be useful to distinguish different MALs, in general it results into a more complicated band structure, as we show in Sec. V A and the SM [55]. Hence, we choose the particle-particle correlation function $g^{(2)}$, which shows a clear signature in its spectrum through which MALs can be more straightforwardly detected.

### C. Transformation properties

In this section, we shortly outline how to derive the transformation properties of $\underline{g}^{(2)}$. Consider an element $h \in G$ of the space group $G$ acting on the electronic operators by a unitary symmetry operator $U_h$. A MAL cluster operator that respects the symmetries of the space group $G$ transforms linearly according to a set of real-space representations $A$ of the space group $G$

$$U_h \hat{O}^{\dagger}_{\boldsymbol{r},\xi} U_h^{-1} = \sum_{\xi'} A^{\boldsymbol{r}}_{\xi'\xi}(h) \hat{O}^{\dagger}_{\boldsymbol{r}',\xi'}, \tag{28}$$

with $\boldsymbol{r}'$ the position of the cluster operator after transformation. As a MAL operator transformed to momentum space, e. g., as in Eq. (4), can only depend on the momentum $\boldsymbol{q}$, it must transform under a consistent representation $\rho^{\boldsymbol{q}}$ of the space

group $G$,

$$U_h \hat{O}^\dagger_{\boldsymbol{q},\xi} U_h^{-1} = \sum_{\xi'} \rho^{\boldsymbol{q}}_{\xi'\xi}(h) \hat{O}^\dagger_{\boldsymbol{q}',\xi'}, \tag{29}$$

with $\boldsymbol{q}' = R\boldsymbol{q}$, $R$ the action of $h$ in momentum space. From this latter expression and Eq. (21), we deduce that $\underline{g}^{(2)}$ transforms under the action of $h$ as

$$\begin{aligned} &\underline{g}^{(2)}_{(\alpha,\beta,\boldsymbol{u}),(\gamma,\delta,\boldsymbol{v})}(\boldsymbol{q}) \\ &\quad = \sum_{(\alpha,\beta,\boldsymbol{u})',(\gamma,\delta,\boldsymbol{v})'} [\rho^{\boldsymbol{q}}(h)_{(\alpha,\beta,\boldsymbol{u})'(\alpha,\beta,\boldsymbol{u})}]^* \\ &\qquad \times \rho^{\boldsymbol{q}}(h)_{(\gamma,\delta,\boldsymbol{v})'(\gamma,\delta,\boldsymbol{v})} \underline{g}^{(2)}_{(\alpha,\beta,\boldsymbol{u})',(\gamma,\delta,\boldsymbol{v})'}(\boldsymbol{q}'), \end{aligned} \tag{30}$$

see the SM [55] for a proof.

## V. CLASSIFICATION OF GREEN'S FUNCTION BAND STRUCTURES

So far, we have introduced the concept of $n$-MALs, and particularly the one of MALs, and we have defined the two-particle radius confined Green's function for general many-body states. In this section, we will bridge the two concepts and see how from the spectrum of $\underline{g}^{(2)}$ we can infer properties of ground states that can be written exactly as MALs, or that can be adiabatically connected to those.

As we mentioned shortly at the end of Sec. IV A, an $n$-particle correlation function $g^{(n)}$ completely determines a state characterized by up to $n$-body correlations. This is exactly what is realized in $n$-MALs, as they are constructed as product states of nonoverlapping $n$-particle operators and therefore confine correlations to engage at most $n$ electrons.

In Sec. V A, we derive the band representations of $\underline{g}^{(2)}$ for MAL states in the limit of a spectrally flattened many-body Hamiltonian. In this simplified scenario, the potential of $\underline{g}^{(2)}$ in diagnosing MAL states properties becomes apparent. In Sec. V B, we propose a framework to derive a full classification of the $\underline{g}^{(2)}$ band representations of the class of MAL states in the limit of spectrally flattened many-body Hamiltonians. Subsequently, in Sec. VI, we explore how this extends to more realistic systems, and we present numerical results for several representative model Hamiltonians in 0D, 1D, and 2D.

### A. Spectrally flattened many-body Hamiltonian limit

As a simplified example to understand the connections between two-particle radius confined Green's functions and MAL states, we compute the spectrum of $\underline{g}^{(1)}$ and $\underline{g}^{(2)}$ in the case of an AL or an MAL ground state, using the spectrally flattened many-body Hamiltonian. The latter is a many-body extension of the concept of "flat band Hamiltonian", or "spectral flattening", used in the context of topological band theory [80]. In the following, we refer to the spectrally flattened many-body Hamiltonian simply as flattened Hamiltonian, for compactness.

The flattened Hamiltonian is defined as

$$\hat{H} = \mathbb{1} - \Delta \, |\mathrm{GS}\rangle \langle \mathrm{GS}| \,, \tag{31}$$

where $|\mathrm{GS}\rangle$ indicates the many-body ground state of the system, with energy $(1-\Delta)$. Any generic many-body state orthogonal to $|\mathrm{GS}\rangle$ has energy 1, hence the system has a many-body gap $\Delta$, which separates the ground state from all excited states. We consider a lattice with a set of unit cells $\Lambda$, where the local Hilbert space of each unit cell is composed of three orbitals, each containing two single-particle states connected by TRS. We label these states by 1, 2, 3 and their TRS partners by $\bar{1}$, $\bar{2}$, $\bar{3}$. The two states belonging to each orbital are related by TRS as follows:

$$\mathcal{T} \hat{c}^\dagger_{\boldsymbol{r},j} \mathcal{T}^{-1} = \hat{c}^\dagger_{\boldsymbol{r},\bar{j}}, \quad \mathcal{T} \hat{c}^\dagger_{\boldsymbol{r},\bar{j}} \mathcal{T}^{-1} = -\hat{c}^\dagger_{\boldsymbol{r},j}, \quad j = 1,2,3. \tag{32}$$

We successively consider the AL ground state

$$|\mathrm{AL}\rangle = \prod_{\boldsymbol{r}\in\Lambda} \hat{c}^\dagger_{\boldsymbol{r},1} \hat{c}^\dagger_{\boldsymbol{r},\bar{1}} \, |0\rangle \,, \tag{33}$$

and the MAL ground state

$$|\mathrm{MAL}\rangle = \prod_{\boldsymbol{r}\in\Lambda} \hat{O}^\dagger_{\boldsymbol{r}} \, |0\rangle = \prod_{\boldsymbol{r}\in\Lambda} \frac{\left(\hat{c}^\dagger_{\boldsymbol{r},1} \hat{c}^\dagger_{\boldsymbol{r},\bar{2}} - \hat{c}^\dagger_{\boldsymbol{r},\bar{1}} \hat{c}^\dagger_{\boldsymbol{r},2}\right)}{\sqrt{2}} \, |0\rangle \,, \tag{34}$$

where we explicitly wrote an expression for the $M^\xi$ coefficients of Eq. (3). From Eqs. (33) and (34), it follows that at a filling of two electrons per unit cell we require two single-particle states to construct an AL, whereas for an MAL operator we require four single-particle states connected pairwise by TRS.

As a basis set of operators entering in $\underline{g}^{(1)}$, we consider the creation and annihilation operators of the three orbitals in each unit cell ($\hat{c}^\dagger_{\boldsymbol{r},j}$, $j = 1,2,3,\bar{1},\bar{2},\bar{3}$, $\forall \boldsymbol{r} \in \Lambda$). As a basis for $\underline{g}^{(2)}$, we consider all the possible products of two such single-particle operators taken at the same $\boldsymbol{r}$, i. e., we set $u_{\max} = 0$. The case of $u_{\max} > 0$ is discussed in the SM [55], where we show that the extension of the radius beyond $u_{\max} = 0$ does not change the universal features in the spectrum of $\underline{g}^{(2)}$ relevant to us [81]. By virtue of the bound in Eq. (24), we separate the flattened Hamiltonian spectrum of $\underline{g}^{(2)}$ into two contributions: the *continuum*, composed by eigenvalues whose inverse lies above or at the many-body gap between the $N$ and $N \pm 2$ sectors of the Hilbert space $\Delta_{\underline{g}^{(2)}}$ ($\lambda_2^{-1} \geqslant \Delta_{\underline{g}^{(2)}} = \Delta$), and the *interaction driven* spectrum of $\underline{g}^{(2)}$, with inverse eigenvalues lying strictly below this gap ($\lambda_2^{-1} < \Delta$). With the considerations that follow, we will reproduce the schematic forms of $\underline{g}^{(1)}$ and $\underline{g}^{(2)}$ already outlined in Figs. 1(e)–1(g).

With the AL in Eq. (33) as a ground state of the flattened Hamiltonian (31), $\underline{g}^{(1)}$ and $\underline{g}^{(2)}$ are diagonal in our chosen basis. The eigenvalues of $\underline{g}^{(1)}$ split into $\lambda_1 = -1/\Delta$ and $\lambda_1 = +1/\Delta$ contributions [see Fig. 3(a)], respectively given by the eigenstates of $\underline{g}^{(1)}$ corresponding to nonoccupied ($\hat{c}^\dagger_{\boldsymbol{r},j}$, $j = 2,\bar{2},3,\bar{3}$) and occupied ($\hat{c}^\dagger_{\boldsymbol{r},j}$, $j = 1,\bar{1}$) single-particle operators in the ground state. By listing all the eigenstates of $\underline{g}^{(1)}$ with positive eigenvalue, the AL ground state can be exactly reconstructed. On the other hand, $\underline{g}^{(2)}$ has a $\lambda_2 = 1/\Delta$ eigenvalue for any two-particle operator obtained from single-particle operators either both occupied or both nonoccupied in the ground state, while it has $\lambda_2 = 0$ for any product mixing an occupied and a nonoccupied single-particle operator [see Fig. 3(c)]. Hence, all eigenvalues of $\underline{g}^{(2)}$ for an AL belong to the continuum spectrum, meaning that it is not possible to

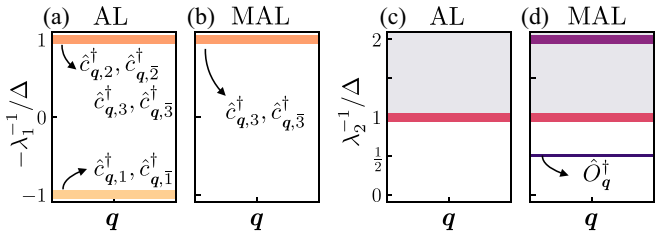


FIG. 3. Green's functions spectra with a spectrally flattened Hamiltonian. [(a),(b)] One- and [(c),(d)] two-particle Green's functions inverse spectra for a AL or MAL ground state, evaluated in the flattened Hamiltonian limit. We plot $-\lambda_1^{-1}$, instead of $\lambda_1^{-1}$ to maintain the analogy with the topological Hamiltonian. Thick lines indicate eigenvalues with multiplicity higher than one, while the thin line in the MAL $\underline{g}^{(2)}$ inverted spectrum indicates a singly degenerate eigenvalue. In (b), there is a band of eigenvalues corresponding to the empty orbitals $3, \bar{3}$ at $-\lambda_1^{-1}/\Delta = 1$, whereas, for comparison, in Fig. 1(g) this line is missing since there are no empty orbitals remaining in the local Hilbert space.

identify the exact form of the AL ground state from the $\underline{g}^{(2)}$ spectrum alone.

Note that the identification of $-[\underline{g}^{(1)}]^{-1}$ with the single-particle Hamiltonian is only justified for a noninteracting Hamiltonian. This is very clear in the flat-band Hamiltonian scenario; since the band structure of $-[\underline{g}^{(1)}]^{-1}$ bears no resemblance with the many-body Hamiltonian. Although the flattened Hamiltonian spectrum as well as the spectrum of $[\underline{g}^{(1)}]^{-1}$ have two levels, their degeneracies are different.

For the MAL ground state of Eq. (34), $\underline{g}^{(1)}$ is again diagonal in our chosen basis, and it has eigenvalues $\lambda_1 = -1/\Delta$ deriving from nonoccupied single-particle operators, and $\lambda_1 = 0$ for any single-particle operator that appears in the ground state [see Fig. 3(b)]. The spectrum of $\underline{g}^{(1)}$ is therefore not useful to determine the exact structure of the MAL ground state. For the MAL state, $\underline{g}^{(2)}$ has a diagonal block, with eigenvalues $\lambda_2 = 1/\Delta$ for eigenstates composed by two nonoccupied operators, and $\lambda_2 = 1/(2\Delta)$ for operators that mix nonoccupied single-particle operators and operators appearing in the MAL state. There is a remaining nondiagonal sector of the $\underline{g}^{(2)}$ matrix spanned by the operators $V_{\boldsymbol{r}} = \{\hat{c}^\dagger_{\boldsymbol{r},1}\hat{c}^\dagger_{\boldsymbol{r},\bar{2}},\ \hat{c}^\dagger_{\boldsymbol{r},\bar{1}}\hat{c}^\dagger_{\boldsymbol{r},2}\}$ (already Pauli antisymmetrized). In this subspace of two-particle operators, $\underline{g}^{(2)}$ assumes the form

$$\underline{g}^{(2)}|_{V_r} = \frac{1}{\Delta}\begin{pmatrix} +1 & -1 \\ -1 & +1 \end{pmatrix}. \tag{35}$$

This leads to a set of eigenvalues $\lambda_2 = 2/\Delta$ belonging to the interaction driven spectrum [see Fig. 3(d)]. The associated eigenstates are given by the two-particle operators $\hat{O}^\dagger_{\boldsymbol{r}}$ appearing in Eq. (34). The block of $\underline{g}^{(2)}$ in Eq. (35) yields another eigenvalue $\lambda_2 = 0$, with eigenstates given by the two-particle operator $(\hat{c}^\dagger_{\boldsymbol{r},1}\hat{c}^\dagger_{\boldsymbol{r}\bar{2}} + \hat{c}^\dagger_{\boldsymbol{r},\bar{1}}\hat{c}^\dagger_{\boldsymbol{r},2})/\sqrt{2}$. Note that the set of eigenvalues discussed above are the same for operators in every decoupled unit cell $\boldsymbol{r}$, leading to a flat band in momentum space.

Importantly, the Fourier transform of the eigenstates of this interaction driven band are exactly the two-particle MAL operators composing the ground state. Hence, the eigenstates of the interaction driven band carry the same transformation properties under the symmetries of the system as the MAL operators of the ground state. We say that an MAL operator *induces* an interaction driven band in the spectrum of $\underline{g}^{(2)}$, meaning that the presence of such an operator in the ground state leads to the existence of a band belonging to the interaction driven spectrum of $\underline{g}^{(2)}$, and the eigenstates of this band are the momentum-space transformed version of the MAL operators of the ground state.

Note that a band belonging to the interaction driven spectrum of $\underline{g}^{(2)}$ can only exist if the ground state is an entangled state, adiabatically disconnected from any single Slater determinant state. This can be understood for instance by considering $\underline{g}^{(2)}$ in real space: When adding or removing a cluster $\hat{O}^\dagger_{\boldsymbol{r}}$ to the ground state of Eq. (34), the resulting state is nonzero in both cases due to the entanglement between the electrons. As both terms in Eq. (21) contribute to the final expectation value, the bound in Eq. (24) can be violated.

As a conclusion of this section, we shortly consider the spectrum of $\underline{g}^{(2)}_{\text{ph}}$, as introduced in Eq. (27), for the AL and MAL states of Eqs. (33) and (34). For the AL ground state, there is no eigenvalue lying in the interaction driven spectrum, which is once more identified as the part of the inverted spectrum falling below $\Delta$, therefore all the eigenvalues lie at either $\lambda^{-1}_{\text{ph}}/\Delta = 1$ or they diverge $\lambda^{-1}_{\text{ph}}/\Delta \to \infty$. In contrast to the case of $\underline{g}^{(2)}$, there is also a divergent eigenvalue $\lambda^{-1}_{\text{ph}}/\Delta = 0$ due to the overlap between the MAL after the action of density-like operators, i. e., of the form $\hat{c}^\dagger_i\hat{c}_i$, with the ground state. For the MAL case, let us first note that the MAL state can be equivalently reexpressed as follows:

$$|\text{MAL}\rangle = \prod_{\boldsymbol{r}\in\Lambda}\begin{cases} \frac{1}{\sqrt{2}}(\hat{c}^\dagger_{\boldsymbol{r},1}\hat{c}_{\boldsymbol{r},\bar{1}} - \hat{c}^\dagger_{\boldsymbol{r},2}\hat{c}_{\boldsymbol{r},\bar{2}})\hat{c}^\dagger_{\boldsymbol{r},\bar{1}}\hat{c}^\dagger_{\boldsymbol{r},\bar{2}}\,|0\rangle \\ \frac{1}{\sqrt{2}}(\hat{c}^\dagger_{\boldsymbol{r},1}\hat{c}_{\boldsymbol{r},2} + \hat{c}^\dagger_{\boldsymbol{r},\bar{1}}\hat{c}_{\boldsymbol{r},\bar{2}})\hat{c}^\dagger_{\boldsymbol{r},2}\hat{c}^\dagger_{\boldsymbol{r},\bar{2}}\,|0\rangle \\ \frac{1}{\sqrt{2}}(\hat{c}^\dagger_{\boldsymbol{r},\bar{2}}\hat{c}_{\boldsymbol{r},\bar{1}} + \hat{c}^\dagger_{\boldsymbol{r},2}\hat{c}_{\boldsymbol{r},1})\hat{c}^\dagger_{\boldsymbol{r},1}\hat{c}^\dagger_{\boldsymbol{r},\bar{1}}\,|0\rangle \\ \frac{1}{\sqrt{2}}(\hat{c}^\dagger_{\boldsymbol{r},\bar{1}}\hat{c}_{\boldsymbol{r},1} - \hat{c}^\dagger_{\boldsymbol{r},\bar{2}}\hat{c}_{\boldsymbol{r},2})\hat{c}^\dagger_{\boldsymbol{r},2}\hat{c}^\dagger_{\boldsymbol{r},1}\,|0\rangle\,. \end{cases} \tag{36}$$

For each of these lines, the operator in parenthesis contributes to the spectrum of $\underline{g}^{(2)}_{\text{ph}}$ with an eigenvalue $\lambda^{-1}_{\text{ph}}/\Delta = 1/2$. In addition, there are two eigenvalues stemming from density-like operators, which appear in the interaction driven part of the spectrum, one with $\lambda^{-1}_{\text{ph}}/\Delta = 1/2$ and another with $\lambda^{-1}_{\text{ph}}/\Delta = 0$, which is divergent due to a nonzero overlap with the ground state when acting with density terms on the MAL state.

Further details on the calculations outlined in this section are discussed in the SM [55].

In summary, from the results obtained in this section we infer that the $\underline{g}^{(1)}$ spectrum is useful in determining the form of an AL ground state, but it is not enough to characterize an MAL. On the other hand, the spectrum of $\underline{g}^{(2)}$ allows to determine the form of an MAL. The $\underline{g}^{(2)}_{\text{ph}}$ spectrum also carries information on the structure of an MAL, although it has an increased complexity.

### B. Classification of $g^{(2)}$ band structures

In this section, we outline how to classify MAL ground states in the limit of a flattened Hamiltonian, based on their $\underline{g}^{(2)}$ spectrum.

Different ALs can be distinguished by their $\underline{g}^{(1)}$ spectrum, as discussed in Sec. IV A, and their classification was already exhausted in the context of TQC. To classify distinct TRS MALs, we solely consider the interaction driven part of the $\underline{g}^{(2)}$ spectrum, which is absent for ALs but appears for MALs with two-particle entanglement.

We define the *interaction driven band representation* of $\underline{g}^{(2)}$ as the collection of representations $\rho_{\boldsymbol{q}}$ of the little groups $G_{\boldsymbol{q}}$ in which the eigenstates of the interaction driven bands of $\underline{g}^{(2)}$ transform. It is only well defined if a gap separating the interaction driven and the continuum spectrum of $\underline{g}^{(2)}$ exists.

The $\underline{g}^{(2)}$ spectrum of any MAL state with a flattened Hamiltonian is obtained by combining the $\underline{g}^{(2)}$ spectra that would result from each two-particle operator in Eq. (3), at a fixed unit cell $\boldsymbol{r}$, taken individually: Every 2-AL operator induces a set of eigenvalues in the continuum spectrum, and every MAL operator disconnected from any AL operator induces an interaction driven band in the spectrum of $\underline{g}^{(2)}$. Hence, in order to fully classify the interaction driven band representations of $\underline{g}^{(2)}$, it is enough to consider all the possible bands induced by states where there is a single MAL cluster operator acting in each unit cell. All the remaining cases can be deduced from the latter by superimposing the bands induced by each MAL cluster operator appearing in the MAL state. We call the minimal set of band representations that span all the possible interaction driven band representations of $\underline{g}^{(2)}$ the *elementary MAL-induced band representations* (EMAL).

In the following, we describe how to obtain the list of EMALs for every space group $G$. We consider a crystalline insulator with space group $G$ and a set of orbitals placed at sites $\boldsymbol{x}_a, \boldsymbol{x}_b, \cdots$ $(a = 1, \cdots, m_1,\ b = 1, \cdots, m_2, \cdots)$ belonging to Wyckoff positions with multiplicities $m_1, m_2, \cdots$, and transforming in a direct sum of representations of the site-symmetry groups $G_{\boldsymbol{x}_a}, G_{\boldsymbol{x}_b}, \cdots$. Interaction driven band representations obtained from orbitals that are placed at non-maximal Wyckoff positions can be adiabatically connected to those at maximal Wyckoff positions without the breaking of any symmetry, hence they do not contribute to generating distinct band representations (see the SM [55]), as it happens in TQC [22]. Therefore, we only consider orbitals placed at maximal Wyckoff positions.

As a first step towards generating a band representation of $\underline{g}^{(2)}$, we need to find all the two-particle local cluster representations $A$ in which two-particle MAL cluster operators transform. These representations are constructed out of the single-particle representations of the orbitals, and have to be compatible with the space group $G$. This aspect is discussed in the SM [55]. This cluster representation induces a representation of $\underline{g}^{(2)}$ in the space group $G$

$$(A \uparrow G) = \rho. \tag{37}$$

Then, the method to classify band representations proceeds as in TQC. To find the band representation induced by $\rho$ at some specific value of the momentum $\boldsymbol{q}$, one has to subduce the representation (37) to the little group $G_{\boldsymbol{q}}$, leading to a two-particle momentum representation

$$(\rho \downarrow G_{\boldsymbol{q}}) = \rho_{\boldsymbol{q}}. \tag{38}$$

The collection of representations (38) at the maximal momenta of the Brillouin zone have to be continuously connected via maximal momentum lines, and this leads to certain compatibility relations. In principle, these compatibility relations need to be solved numerically using a graph theory algorithm [22].

This way, all the possible band representations induced by MAL states compatible with the space group $G$ have been listed, provided that the list of $A$ representations is exhaustive. By comparing the band representation of a Green's function of interest to the such constructed band representations, in the limit of flattened Hamiltonian and by restricting the ground states to the class of MAL states, iTQC provides a new definition of topological states: *If the band representation associated to the interaction-driven spectrum of a Green's function cannot be induced from ALs and 2-MALs, the state is either (i) an SPT that cannot be induced from 0-dimensional blocks or (ii) it is a many-body state that is dominated by many-body correlations that involve more than two electrons.*

In Sec. V C, we discuss the full classification of EMALs in 1D, which gives an explicit example of the procedure outlined above. In addition, simple 2D examples where the classification can be done by hand are discussed in the SM [55], and in future work we plan to compile the full tables for all 2D and 3D space groups.

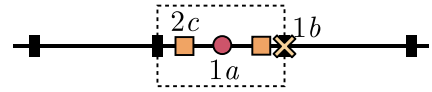


FIG. 4. One-dimensional lattice. Wyckoff positions of a 1D lattice. The inversion center coincides with the Wyckoff position 1$a$.

### C. Complete classification of ALs and MALs in 1D

One-dimensional systems are already an interesting testing ground for our formalism. Within TQC, they only allow for trivial phases. These are either ALs or obstructed ALs, for which the atomic positions do not coincide with the Wyckoff positions of the AL Wannier functions. An example for the latter is the Su-Schrieffer-Heeger model for spinful electrons [82]. With interactions, however, it is possible to find phases described by MALs. In Sec. VI B, we provide a 1D model and demonstrate how iTQC can be used to identify different phases.

In 1D crystals there are three Wyckoff positions: 1$a$, 1$b$, and 2$c$ (Fig. 4), and as ALs and MALs operators placed at 2$c$ are adiabatically connected to the ones placed at 1$a$ and 1$b$, these cases can be discarded. In this section, we consider only inversion symmetry among the spatial crystalline symmetries, since different AL phases are not mirror indicated in 1D TRS crystals. The site symmetry groups of the sites at Wyckoff positions 1$a$ and 1$b$ are isomorphic to $C_i$. Hence, the relevant point group is the double group of $C_i$ (No. 2), and it contains the identity ($E$), inversion ($\mathcal{I}$), $2\pi$ rotation ($\bar{E}$), and the double inversion ($\bar{E}\mathcal{I}$) operations [83]. This group has four 1D irreps:

the spinless [$\mathrm{Tr}\rho(\bar{E}) = +1$] representations $A_g$ and $A_u$, and the spinful [$\mathrm{Tr}\rho(\bar{E}) = -1$] representations $\bar{A}_g$ and $\bar{A}_u$, where the subscript $g$ ($u$) indicates that the representation is even (odd) under inversion (see Table S1 in the SM [55]).

Hence, the site symmetry groups of the sites at Wyckoff positions $1a$ and $1b$ both admit two types of spinful orbitals, either with physical irrep even ($\bar{A}_g\bar{A}_g$) or odd ($\bar{A}_u\bar{A}_u$) under inversion, which are often simply referred to as $s$ and $p$ orbitals [84]. The corresponding creation operators acting in momentum space are labeled by $\hat{c}^\dagger_{k,\alpha}$, with $\alpha = (W, \tau, \sigma)$. Here, $\tau \in \{\bar{A}_g\bar{A}_g, \bar{A}_u\bar{A}_u\}$ indicates the spinful orbital representation of the site-symmetry group $G_{\boldsymbol{x}}$ of a site $\boldsymbol{x}$ at Wyckoff positions $W \in \{1a, 1b\}$, and $\sigma \in \{\uparrow, \downarrow\}$ is the spin degree of freedom, which enumerates the two states connected by TRS in each orbital.

The action of inversion and TRS on the orbitals transforming in the two possible $\tau$ irreps is

$$\tau_{\sigma'\sigma}(\mathcal{I}) = \pm\mathbb{1}_{\sigma'\sigma}, \quad \tau_{\sigma'\sigma}(\mathcal{T}) = \mathrm{i}\sigma^{(2)}_{\sigma'\sigma}, \tag{39}$$

where the plus sign holds for $\tau = \bar{A}_g\bar{A}_g$ and minus sign for $\tau = \bar{A}_u\bar{A}_u$. Note that inversion acts trivially on the spin degree of freedom. The site symmetry group representation in momentum space induces the Wyckoff position-dependent representations at momentum $q$, which read

$$\rho^q_{1a}(\mathcal{I}) = 1, \quad \rho^q_{1b}(\mathcal{I}) = e^{\mathrm{i}q}, \tag{40}$$

for inversion, while TRS acts by complex conjugation.

After having listed the allowed single-particle representations $\tau$, we need to find the representations of two-particle operators consistent with the space group and constructed from single-particle state representations. In general, this task can be rather cumbersome, but it is enough to narrow down the search to some restricted cases to obtain a full classification of EMALs in 1D: we only consider MAL operators constructed out of single-particle operators that are placed at the same (maximal) Wyckoff position and same unit cell. Then, the local cluster representation $A$ is obtained by taking tensor products of pairs of the single-particle representations $\tau$, and the two-particle representation $\rho$ becomes the tensor product between $A$ and the momentum space representations induced by the site symmetry groups (40) (see the SM [55]). The relevant multiplication rules are $\bar{A}_g \otimes \bar{A}_g = \bar{A}_u \otimes \bar{A}_u = A_g$, and $\bar{A}_g \otimes \bar{A}_u = A_u$. Explicitly, the possible $A$ representations are given by

$$\begin{aligned}
(\bar{A}_g\bar{A}_g) \otimes (\bar{A}_g\bar{A}_g) &= A_g \oplus A_g \oplus A_g \oplus A_g,\\
(\bar{A}_u\bar{A}_u) \otimes (\bar{A}_u\bar{A}_u) &= A_g \oplus A_g \oplus A_g \oplus A_g,\\
(\bar{A}_g\bar{A}_g) \otimes (\bar{A}_u\bar{A}_u) &= A_u \oplus A_u \oplus A_u \oplus A_u,
\end{aligned} \tag{41}$$

for both the Wyckoff positions $1a$ and $1b$. Each tensor product in (41) is four-dimensional and splits into a 1D spin-0 and a 3D spin-1 sector. The constraints of TRS and uniqueness of the ground state single out the spin-0 sector, as it is the only nondegenerate representation appearing in the presence of $SU(2)$ symmetry, leaving only a single term, out of four, in each line of Eq. (41). For the spin-1 sector, three 1D representations should be filled to fulfill $SU(2)$ symmetry, leading to an AL state. This leaves us with two possible types of $A$ representation, $A_g$ or $A_u$, irrespective of whether we consider orbitals at $1a$ or $1b$.

To obtain the full two-particle representation $\rho$, we consider the tensor product between local cluster spin-singlet irreps $A$ and one of the momentum space representation $\rho^q_W$ of Eq. (40), depending on whether the orbitals are placed at the $1a$ or $1b$ Wyckoff position sites. This leads to the two-particle representations

$$\rho_{W,A_g} = A_g \otimes \rho^q_W, \quad \rho_{W,A_u} = A_u \otimes \rho^q_W, \tag{42}$$

with $W \in \{1a, 1b\}$.

The two-particle representations are labeled by the $A$ representation from which they originate and the position of the two orbitals, which is unique as the two single orbital locations coincide.

To give an explicit example, we write an MAL operator transforming in the $\rho_{1a,A_u}$ representation, subduced to a specific momentum $q$, as

$$\begin{aligned}
\hat{O}^\dagger_{q,1a,A_u} = \frac{1}{\sqrt{2N}} \sum_k \big(&\hat{c}^\dagger_{k,1a,\bar{A}_g\bar{A}_g,\uparrow}\hat{c}^\dagger_{-k+q,1a,\bar{A}_u\bar{A}_u,\downarrow}\\
&- \hat{c}^\dagger_{k,1a,\bar{A}_g\bar{A}_g,\downarrow}\hat{c}^\dagger_{-k+q,1a,\bar{A}_u\bar{A}_u,\uparrow}\big),
\end{aligned} \tag{43}$$

with $N$ the number of unit cells in the 1D lattice.

Based on the set of 1D two-particle representations of Eq. (42), the list of EMALs for the 1D space group with inversion ($\bar{1}$) can be inferred. Table II lists the irrep of the $\underline{g}^{(2)}$ interaction driven bands at the maximal momenta $\Gamma$ ($k = 0$) and $X$ ($k = \pi$) of the Brillouin zone, obtained by subducing the representation $\rho$ of each MAL operator to the little groups $G_\Gamma$ and $G_X$. Note that some of the EMALs can be induced by a 2-AL operator (e. g., $\hat{O}^\dagger_{1a,A_g}$), while others cannot be obtained by any 2-AL operator (e. g., $\hat{O}^\dagger_{1a,A_u}$). This follows from the fact that some of the MALs can be adiabatically connected to ALs without the breaking of any relevant symmetry of the crystal point group, and by tuning off interactions in the system, while there are intrinsically interacting MALs disconnected from any noninteracting state.

In 1D, the MAL classification exhausts all the possibilities in terms of inversion eigenvalues at maximal momenta, meaning that any single interaction driven band representation of $\underline{g}^{(2)}$ is equivalent to one of the EMALs listed in Table II. For a state constructed as a product of more than one MAL operator per unit cell, there will be multiple interaction driven bands in the spectrum of $\underline{g}^{(2)}$, each one described by one of the band representations of Table II. However, states not adiabatically connected to MALs or ALs will not be captured by this classification, and may for instance result in a number of interaction driven bands, which is not compatible with the number of predicted interaction driven bands at the same filling.

In 2D, the classification is richer, and MALs do not realize all the possible combinations of representations at maximal points, in principle allowing for topologically nontrivial band representations in $\underline{g}^{(2)}$, or, once more, for bands that are not captured by the MAL ansatz.

## VI. NUMERICAL RESULTS

So far, we have only made statements on the classification of MALs in the limit of a flattened Hamiltonian. With more

TABLE II. MAL band representation in 1D. The first column lists all the labels of the two single-particle representations $\tau$, $\tau'$ whose tensor products give rise to an allowed two-particle representation $\rho$. The resulting $\rho$'s labels are listed in the second column. The columns for the $\underline{g}^{(2)}$ representations contain the representations of the lowest lying band in $\underline{g}^{(2)}$ obtained by subducing $\rho$ to the maximal momenta $\Gamma$ and $X$. In the last two columns, the irreps of the lowest lying bands of the particle-hole Green's function $\underline{g}^{(2)}_{\text{ph}}$ are listed, see Sec. V A and the SM [55], and the contribution of the trivial zero eigenvalue is removed.

| | | $\underline{g}^{(2)}$ | | $\underline{g}^{(2)}_{\text{ph}}$ | |
|---|---|---|---|---|---|
| $\tau \otimes \tau'$ | $\rho$ | $\Gamma$ | $X$ | $\Gamma$ | $X$ |
| $(1a, \bar{A}_g\bar{A}_g) \otimes (1a, \bar{A}_g\bar{A}_g), (1a, \bar{A}_u\bar{A}_u) \otimes (1a, \bar{A}_u\bar{A}_u)$ | $1a, A_g$ | $\Gamma_1^+$ | $X_1^+$ | $\bigoplus_{i=1}^{5} \Gamma_1^+$ | $\bigoplus_{i=1}^{5} X_1^+$ |
| $(1b, \bar{A}_g\bar{A}_g) \otimes (1b, \bar{A}_g\bar{A}_g), (1b, \bar{A}_u\bar{A}_u) \otimes (1b, \bar{A}_u\bar{A}_u)$ | $1b, A_g$ | $\Gamma_1^+$ | $X_1^-$ | $\bigoplus_{i=1}^{5} \Gamma_1^+$ | $\bigoplus_{i=1}^{5} X_1^-$ |
| $(1a, \bar{A}_g\bar{A}_g) \otimes (1a, \bar{A}_u\bar{A}_u)$ | $1a, A_u$ | $\Gamma_1^-$ | $X_1^-$ | $\bigoplus_{i=1}^{3} \Gamma_1^+ \bigoplus_{i=1}^{2} \Gamma_1^-$ | $\bigoplus_{i=1}^{3} X_1^+ \bigoplus_{i=1}^{2} X_1^-$ |
| $(1b, \bar{A}_g\bar{A}_g) \otimes (1b, \bar{A}_u\bar{A}_u)$ | $1b, A_u$ | $\Gamma_1^-$ | $X_1^+$ | $\bigoplus_{i=1}^{3} \Gamma_1^+ \bigoplus_{i=1}^{2} \Gamma_1^-$ | $\bigoplus_{i=1}^{3} X_1^- \bigoplus_{i=1}^{2} X_1^+$ |

realistic Hamiltonians, our conclusions obtained in the idealized scenario of Sec. V A no longer hold exactly. However, our numerical calculations show that as long as the ground state is a gapped state adiabatically connected to an MAL and dominated by two-body correlations, the spectrum of $\underline{g}^{(2)}$ still conveys information on the properties of the ground state. This indicates that the spectrum of $\underline{g}^{(2)}$ is a powerful tool that can be useful beyond the perturbative regime of small interaction strength.

Away from the ideal limit, the interaction driven bands predicted in the flattened Hamiltonian limit show a momentum dependence, while still retaining their symmetry properties and a gap separation from the bands characterized by larger eigenvalues. The lowest bands in the spectrum of $[\underline{g}^{(2)}]^{-1}$ may not necessarily lie below the bound (24), but still retain a gap separation from the remaining bands. Conversely, the presence of these bands in the spectrum of $[\underline{g}^{(2)}]^{-1}$ hints at a ground state that is either closely approximated by an MAL state or adiabatically connected to an MAL state and still dominated by two-body correlations, rather than correlations involving a higher number of particles.

In our numerical calculations, we find that this signature of MAL ground state is robust at large values of the interaction strength, as long as the many-body Hamiltonian remains fully gapped and the ground state is dominated by two-body correlations rather than higher-order correlations. Therefore we speak of *MAL phases* to indicate a phase of a system where the ground state can be adiabatically connected to an MAL but not to any AL, without any gap closings or the breaking of symmetries of the system. On the other hand, we say a system is in an AL phase, when its ground state can be adiabatically connected to an AL, without gap closings or symmetry breaking.

In this section, we will present a series of numerical calculations for different model Hamiltonians where the considerations of Sec. V still hold for a range of parameters. These examples showcase how the classification of the interaction driven band representations of $\underline{g}^{(2)}$ can be used to infer properties of certain interacting ground states, beyond the limit of flattened Hamiltonian or MAL state.

We will first discuss the Hubbard square (Sec. VI A), which realizes a 0D MAL state in the limit of vanishing interactions. We then study two examples where the Hubbard square is used as a building block to construct first a 1D lattice, the Hubbard diamond chain (Sec. VI B), and then a 2D checkerboard lattice (Sec. VI C). As a last model, we present another example of 0D Hubbard cluster, the Hubbard star of David (Sec. VI D), which may find application in the context of the layered material $1T - TaS_2$ [85]. The four schematics of the models considered throughout this section are shown in Fig. 5.

For each model presented in the following sections, we use symmetry groups that contain a minimal set of symmetries that allow to distinguish the various phases appearing in the

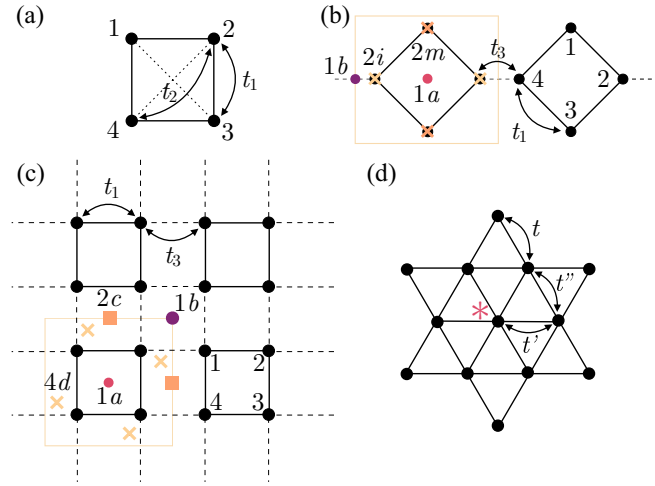


FIG. 5. Schematics of the models considered. Schematics of (a) the Hubbard square (Sec. VI A), (b) the Hubbard diamond chain (Sec. VI B), (c) the checkerboard lattice of Hubbard squares (Sec. VI C), and (d) the star of David cluster (Sec. VI D). In (b) and (c) some Wyckoff positions are explicitly marked for the two lattices, and the unit cell is highlighted by the yellow rectangle. The tunneling amplitudes discussed in the various models are highlighted in each schematic.

phase diagrams, rather than the full symmetry groups. This choice is motivated by the aim of keeping the notation simple, since considering the full symmetry group would lead to a more complicated analysis while the results would remain substantially unchanged.

There are several numerical techniques, which enable one to calculate the two-particle Green's function $\underline{g}^{(2)}$, such as exact diagonalization (ED) and QMC. In this section we will focus on systems amenable to these two techniques. In principle, these numerical techniques are also useful in the computation of $n$-particle Green's functions with generic $n$. A more detailed discussion on the numerical calculations whose results are shown in the following sections is presented in the SM [55].

Importantly, the QMC results presented in Sec. VI C exemplify how different SPT phases can be distinguished by means of $\underline{g}^{(2)}$ for system sizes beyond the reach of methods such as ED and DMRG. While ED and DMRG provide access to the full many-body ground state, in our formulation the knowledge of the ground state is not required, nor the calculation of correlation functions involving an extensive number of electronic operators. This has to be contrasted with conventional techniques developed to diagnose SPT phases, such as the evaluation of string-order parameters [70] and partial symmetry operations applied to subsystems of size comparable with the total size of the system [66,67,69]. Both of these approaches to obtain SPT invariants involve an extensive number of fermionic and swap operators, respectively, which can be obtained efficiently when the ground state is known and in 1D systems [70], but become computationally inaccessible in more than 1D and as the size grows. In addition, canonical pgSPT and cSPT invariants are quantized [66,67,69], and therefore it is reasonable to expect that their value heavily suffers from finite-size effects. Our method is still applicable for modest system sizes, as it only requires the presence of a gap in the many-body and in the $\underline{g}^{(2)}$ spectrum, while it does not rely on a quantized response.

### A. Hubbard square

As a 0D numerical example, we compute the $\underline{g}^{(2)}$ spectrum in ED for the Hubbard square, a four-site interacting fermionic model studied in Refs. [53,86–88]. A spinful electron is placed at each site of the square [89], and the Hamiltonian is defined as

$$\hat{H}_{\rm HS} = -t_1 \sum_{i=1}^{4}\sum_{\sigma}(\hat{c}^\dagger_{i,\sigma}\hat{c}_{i+1,\sigma} + \text{H.c.}) + t_2 \sum_{i=1}^{4}\sum_{\sigma}\hat{c}^\dagger_{i\sigma}\hat{c}_{i+2,\sigma} + U\sum_{i=1}^{4}\left(\hat{n}_{i,\uparrow}-\frac{1}{2}\right)\left(\hat{n}_{i,\downarrow}-\frac{1}{2}\right), \tag{44}$$

with $\hat{c}^\dagger_{i\sigma}$ ($\hat{c}_{i\sigma}$) creating an electron at site $i = 1,\ldots,4$, with the spin $\sigma \in \uparrow,\downarrow$ labeling the two single-particle states of each orbital. It is convenient to transform the single-particle states in eigenstates of the fourfold rotation operation ($C_4$),

$$\hat{c}^\dagger_{\ell,\sigma} = \frac{1}{2}\sum_{j=1}^{4} e^{\mathrm{i}\ell j}\hat{c}^\dagger_{j,\sigma}, \quad \hat{c}_{\ell,\sigma} = \frac{1}{2}\sum_{j=1}^{4} e^{-\mathrm{i}\ell j}\hat{c}_{j,\sigma}, \tag{45}$$

with eigenvalues $\ell \in \{0, \frac{\pi}{2}, \pi, -\frac{\pi}{2}\}$. The Hamiltonian becomes

$$\hat{H}_{\rm HS} = \sum_{\ell,\sigma}\left(\varepsilon(\ell) - \mu - \frac{U}{2}\right)\hat{c}^\dagger_{\ell,\sigma}\hat{c}_{\ell,\sigma} + \frac{U}{N}\sum_{\ell,\ell',\ell''}\hat{c}^\dagger_{\ell,\uparrow}\hat{c}^\dagger_{\ell',\downarrow}\hat{c}_{\ell''+\ell,\downarrow}\hat{c}_{-\ell''+\ell',\uparrow}, \tag{46}$$

with $\varepsilon(\ell) = -2t_1\cos(\ell) + t_2\cos(2\ell)$, and $N = 4$ the number of sites. The $C_4$ symmetric electronic single-particle states transform as

$$C_4\hat{c}^\dagger_{\ell,\sigma}C_4^{-1} = \sum_{\sigma'} e^{\mathrm{i}(\ell+\frac{\pi}{4}\sigma^{(3)}_{\sigma\sigma'})}\hat{c}^\dagger_{\ell,\sigma'}. \tag{47}$$

The minimal symmetry group to distinguish the phases of the Hubbard square is the double group $C_4^D$ (see Table S3 within the SM [55]), and the eight $\hat{c}^\dagger_{k,\sigma}$ operators transform as a set of double-valued physical representations of $C_4^D$ (see the SM [55]). Focusing on the case of half-filling, the Hubbard square is characterized by two distinct phases: trivial ($t_2 > t_1$) and nontrivial ($t_2 < t_1$).

In the limit of $U/t_1 \to 0$, the ground state of the trivial phase is a gapped state of the single Slater determinant form

$$|\mathrm{T}\rangle = \hat{c}^\dagger_{\frac{\pi}{2},\uparrow}\hat{c}^\dagger_{\frac{\pi}{2},\downarrow}\hat{c}^\dagger_{-\frac{\pi}{2},\uparrow}\hat{c}^\dagger_{-\frac{\pi}{2},\downarrow}|0\rangle\,. \tag{48}$$

This wave function transforms under the trivial representation of the point group ($A$), meaning $C_4|\mathrm{GS}\rangle = +|\mathrm{GS}\rangle$. In the limit $U/t_2 \to \infty$ the wave function takes an alternative form with the same $C_4$ eigenvalue,

$$|\mathrm{T}'\rangle = \hat{O}^\dagger_{13}\hat{O}^\dagger_{24}|0\rangle, \tag{49}$$

where $\hat{O}^\dagger_{ij} \equiv [c^\dagger_{i,\uparrow}c^\dagger_{j,\downarrow} + c^\dagger_{j,\uparrow}c^\dagger_{i,\downarrow}]/\sqrt{2}$. The states $|\mathrm{T}\rangle$ and $|\mathrm{T}'\rangle$ can be continuously connected as they are characterized by the same $C_4$ symmetry eigenvalues.

For the nontrivial phase, in the limit of $U/t_1 \to 0$, the square has the unique ground state

$$|\mathrm{NT}\rangle = \frac{1}{\sqrt{2}}\hat{c}^\dagger_{0,\uparrow}\hat{c}^\dagger_{0,\downarrow}(\hat{c}^\dagger_{\frac{\pi}{2},\uparrow}\hat{c}^\dagger_{\frac{\pi}{2},\downarrow} + \hat{c}^\dagger_{-\frac{\pi}{2},\uparrow}\hat{c}^\dagger_{-\frac{\pi}{2},\downarrow})\,|0\rangle\,, \tag{50}$$

and in the limit $U/t_1 \to \infty$

$$|\mathrm{NT}'\rangle = \frac{1}{\sqrt{3}}[\hat{O}^\dagger_{12}\hat{O}^\dagger_{34} - \hat{O}^\dagger_{14}\hat{O}^\dagger_{23}]\,|0\rangle\,, \tag{51}$$

where both states have $C_4|\mathrm{GS}\rangle = -|\mathrm{GS}\rangle$, and transform in the $B$ representation of the point group (see the SM [55]). The state in Eq. (50) realizes an example of MAL, with a $C_4$ eigenvalue that is nontrivial, in the sense that it cannot be reproduced by any TRS AL. For this state, there is a single MAL cluster operator that leads to a contribution in the interaction driven spectrum of $g^{(2)}$, the one enclosed in parenthesis in Eq. (50). Once more, the states $|\mathrm{NT}\rangle$ and $|\mathrm{NT}'\rangle$ can be continuously connected as they have the same eigenvalue under $C_4$ operation.

Figure 6 shows the ED inverse $\underline{g}^{(2)}$ spectra obtained in the two phases, trivial [Fig. 6(a)] and nontrivial [Fig. 6(b)], for a range of interaction strength $U/t_1$. From the spectra of $\underline{g}^{(2)}$, we find that in each of the two phases there is a single eigenvalue below the two-particle gap $\Delta_{\underline{g}^{(2)}}$, for $U/t_1$ not too large, whose symmetry eigenvalue under the action of

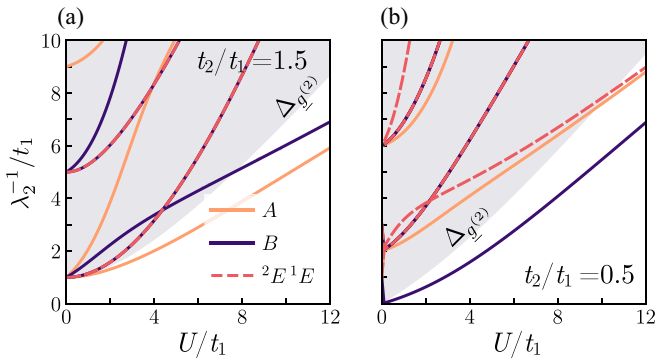


FIG. 6. Hubbard square. Inverse eigenvalues of the two-particle Green's function for (a) the trivial phase ($t_2 > t_1$) and (b) the nontrivial phase ($t_2 < t_1$) of the Hubbard square (44). The boundary of the region shaded in yellow marks the two-particle gap $\Delta_{\underline{g}^{(2)}}$ at each value of the Hubbard interaction strength $U$. The eigenvalues of $\underline{g}^{(2)}$ are colored according to the legend in (a), with the color code distinguishing the $C_4^D$ representation in which their eigenstates transform, either $A$, $B$ or the corepresentation $^1E\,^2E$, see Table S3 within the SM [55]. Solid (dashed) lines indicate singly (doubly) degenerate eigenvalues. The state in (b) below $\Delta_{\underline{g}^{(2)}}$ transforming in the $B$ irrep of $C_4$ indicates the nontrivial MAL character of the ground state. All quantities are expressed in units of $t_1$.

$C_4$ rotation reflects the symmetry of the ground state. As $U$ becomes increasingly larger, the relevant correlation function describing the Hubbard square state becomes the four-particle correlation function. Hence, additional eigenvalues begin to appear in the lower part of the inverted spectrum of $\underline{g}^{(2)}$.

Larger "Hubbard molecules" can exhibit even more complex phase diagrams of band insulating and fragile Mott insulating phases [90]. In Sec. VI D, we present an example of larger cluster, the Hubbard star of David, where we observe a rich phase diagram that includes an MAL phase.

### B. Hubbard diamond chain

As a 1D example, we consider the Hubbard diamond chain defined in Ref. [54]. This is constructed by connecting several Hubbard squares through their corners, see Fig. 5(b). In this case, the relevant space group is *Pmmm* (No. 47), and the lattice sites are placed at the $2m$ and $2i$ Wyckoff positions. The site-symmetry groups of sites in Wyckoff position $2m$ and $2i$ are isomorphic to $m2m$ and $2mm$, respectively, and the orbitals localized at these four sites can be continuously connected to orbitals placed at the maximal Wyckoff position $1a$ of the lattice. Here, we only consider the point group $C_{2v}$ as it is sufficient in diagnosing the MAL phase (while in Ref. [54] the analysis is carried out for the full symmetry group $D_{2h}$). As for the Hubbard square, each site has spinful electrons. The Hamiltonian is

$$\hat{H} = U\sum_{j,\alpha}\hat{n}_{j,\alpha,\uparrow}\hat{n}_{j,\alpha,\downarrow} + \sum_{j,\sigma}\sum_{\alpha,\beta}\hat{c}^{\dagger}_{j,\alpha,\sigma}\mathbb{T}_{\alpha\beta}\hat{c}_{j,\beta,\sigma} - \sum_{\sigma,j}(t_3\hat{c}^{\dagger}_{j,1,\sigma}\hat{c}_{j+1,3,\sigma} + \text{h.c.}) - \mu\sum_{j,\alpha,\sigma}\hat{n}_{j,\alpha,\sigma}, \quad (52)$$

with

$$\mathbb{T} = -\begin{bmatrix} 0 & t_1 & t_2 & t_1 \\ t_1 & 0 & t_1 & t_2 \\ t_2 & t_1 & 0 & t_1 \\ t_1 & t_2 & t_1 & 0 \end{bmatrix}, \quad (53)$$

where $\hat{c}^{\dagger}_{j,\alpha,\sigma}(\hat{c}_{j,\alpha,\sigma})$ creates (annihilates) an electron of spin $\sigma$ at site $\alpha \in \{1, 2, 3, 4\}$ of the cell labeled by $j = 1, \ldots, N$, with $N$ the number of unit cells. In Eq. (52), $t_1$ and $t_2$ are hopping amplitudes within a single square, $t_3$ the one between different squares, and $\mu$ is the chemical potential.

The noninteracting model at half-filling has three phases [54]: If the hopping $t_2$ dominates, then the individual squares are in the trivial phase of the Hubbard square. This is an insulating AL state. If the hopping $t_3$ dominates, then the model can be adiabatically connected to the interacting SSH chain [82], with the addition of two weakly coupled sites. This insulating state is an obstructed AL. These two insulating states will be unaffected by a small $U$ since they are protected by a gap. In fact, it is known that there is no phase transition as a function of $U$ for both the SSH chain [75] and the trivial phase of the Hubbard square [53], it therefore is plausible that there is no phase transition as a function of $U$ in these phases of the Hubbard diamond chain. On the other hand, if $t_1$ dominates, then the individual squares can be described by the nontrivial phase of the Hubbard square. For $U = 0$ this phase is metallic, but for any finite $U$ a gap in the many-body spectrum opens up, analogously with the case of the isolated Hubbard square. Therefore, the system realizes an MAL phase at finite $U$ and dominant $t_1$.

We perform ED and QMC calculations on the system at $t_2 = 0$, while varying $t_3/t_1$ and $U/t_1$. In Fig. 7(a), the phase diagram of the system as a function of these two parameters is shown: At $U = 0$ the system is gapless (therefore we label it as metal), at large $U/t_1$ and small $t_3/t_1$ the ground state is described by an MAL state, and at small $U/t_1$ and large $t_3/t_1$ the system realizes an antiferromagnetic (AFM) phase. Figures 7(b)–7(e) show the $\underline{g}^{(1)}$ and $\underline{g}^{(2)}$ inverse spectra for the case of $u_{\max} = 6$, with the unit cell defined as a single diamond [see Fig. 5(b)]. In the MAL regime, corresponding to Fig. 7(d), there is a single low-lying band in the inverted spectra of $\underline{g}^{(2)}$, whose eigenstates have mirror $M_y$ eigenvalue equals to $-1$ at both momenta $q = 0, \pi$. This signals that the ground state is adiabatically connected to an MAL placed at the $1a$ Wyckoff position of the unit cell, transforming in the $A_2$ irrep of the point group $C_{2v}^D$. On the other hand, in the large $t_3$ regime of Fig. 7(e), there is no band in the spectrum of $[\underline{g}^{(2)}]^{-1}$ separated from the continuum.

### C. Checkerboard lattice of Hubbard squares

As a 2D example, we consider the model proposed in Ref. [53]. This consists of a checkerboard lattice where Hubbard squares, with on-site interaction $U$ and nearest-neighbor hopping $t_1$, are coupled to the neighboring unit cell by a hopping parameter $t_3$, see Fig. 5(c). The Hamiltonian for the model reads

$$\hat{H} = \sum_{\boldsymbol{r}}\hat{H}_{\text{HS},\boldsymbol{r}} - \sum_{\substack{\langle \boldsymbol{r},i,\boldsymbol{r}',j\rangle \\ \boldsymbol{r}\neq\boldsymbol{r}'}}\sum_{\sigma} t_3(\hat{c}^{\dagger}_{\boldsymbol{r},i,\sigma}\hat{c}_{\boldsymbol{r}',j,\sigma} + \text{H.c.}), \quad (54)$$

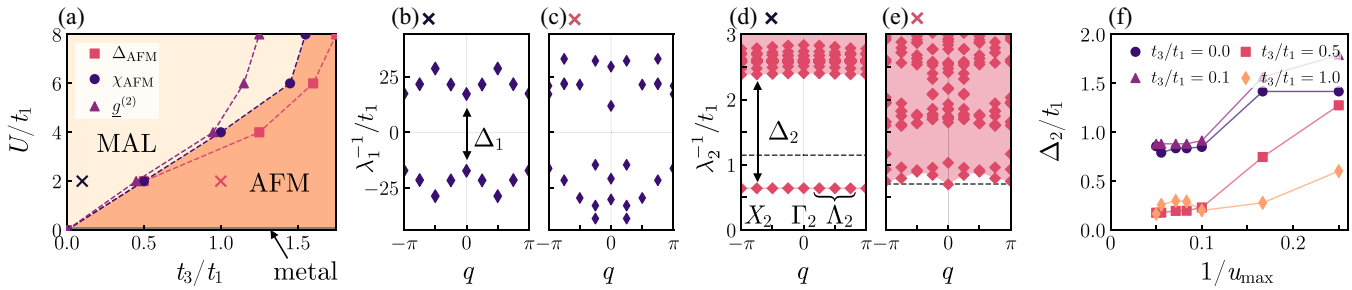


FIG. 7. Hubbard diamond chain. (a) Phase diagram of the diamond chain model in the $(U/t_1, t_3/t_1)$ plane. In the upper part, the system is in an MAL phase, while in the lower it is in an AFM phase. The phase transition is marked using three approaches: (i) $\Delta_{\rm AFM}$, by the vanishing gap between the ground state and the $S = 1, k = \pi$ excited state computed within $L \to \infty$ extrapolation of the QMC data; (ii) $\chi_{\rm AFM}$, inflection point in susceptibility towards the respective Néel order computed within QMC on $L = 10$ unit cells; and (iii) $\underline{g}^{(2)}$, by the vanishing gap between the lowest-lying band and the rest of the inverted spectrum of $\underline{g}^{(2)}$, computed within QMC on the $L = 8$ chain (see the SM [55]). The two crosses mark the points in the phase diagram corresponding to the plots (b)–(e). [(b),(c)] Inverted band structure of $\underline{g}^{(1)}$ of the diamond chain obtained using QMC simulations, computed at $U/t_1 = 2$ and $t_3/t_1 = 0.1,\ 1.0$, for (b) and (c) respectively. The spectrum is doubly degenerate at each value of $q$ due to the spin degree of freedom. [(d),(e)] Inverted band structure of $\underline{g}^{(2)}$, for $U/t_1 = 2$, $u_{\rm max} = 6$, $L = 8$ and $t_3/t_1 = 0.1,\ 1.0$, for (c) and (d), respectively. The dashed line indicates the two-particle gap $\Delta_{\underline{g}^{(2)}}$ estimated from the spectral gap of $[\underline{g}^{(1)}]^{-1}$, meaning $\Delta_{\underline{g}^{(2)}} \approx 2\Delta_1$. (f) Spectral gap $\Delta_2$ between the lowest-lying and the remaining eigenvalues of $[\underline{g}^{(2)}]^{-1}$, as a function of $1/u_{\rm max}$, computed at fixed $U/t_1 = 2$, and $t_3/t_1 = 0.0,\ 0.1,\ 0.5$, and 1.0.

with $\boldsymbol{r}, \boldsymbol{r}'$ labeling different unit cells, $i, j \in \{1, \cdots, 4\}$ indicating the sites within each unit cell, and $H_{{\rm HS},\boldsymbol{r}}$ is the Hamiltonian in Eq. (44) for the square in the unit cell labeled by $\boldsymbol{r}$. Here, we neglect the diagonal hopping $t_2$ in Eq. (44) as our focus is on the nontrivial phase of the Hubbard square.

In the limit $t_1 \gg t_3$ and $U \to 0$, the ground state is described by a product of MAL operators, each transforming in the $B$ representation of the point group $C_4^D$ and placed at the Wyckoff position $1a$ of the lattice. In the opposite regime of dominating $t_3$ ($t_1 \ll t_3$ and $U \to 0$) the ground state is also described by a product of MAL operators transforming in the $B$ representation of $C_4^D$, which are, however, placed at the $1b$ Wyckoff position of the lattice. Therefore, at finite $U$, the two regimes of dominating $t_1$ or dominating $t_3$ realize two distinct MAL phases. For the intermediate region $t_1 \approx t_3$, the ground state is an AFM at finite $U$ and is gapless (metal) at $U = 0$. The two MAL phases can be distinguished by the band representations that the distinct MALs induce in the spectrum of $\underline{g}^{(2)}$. Figures 8(b)–8(d) show the inverted spectrum of $\underline{g}^{(2)}$ in the three phases. For the two MAL phases, the irreps of the lowest-lying bands at maximal momenta in the Brillouin zone are marked, and they correspond to the band representation induced by an MAL cluster transforming in the $B$ representation of $C_4^D$ placed respectively at the $1a$ and $1b$ Wyckoff position. In the SM [55], we explicitly derive the full band representation induced by MAL operators placed at the $1a$ Wyckoff position. The case in which the orbitals are placed at the $1b$ Wyckoff position follows analogously.

### D. Hubbard star of David

As a last example of application of our method, we consider a single cluster of atomic sites forming a star of David shape. This model is motivated by the monolayer material

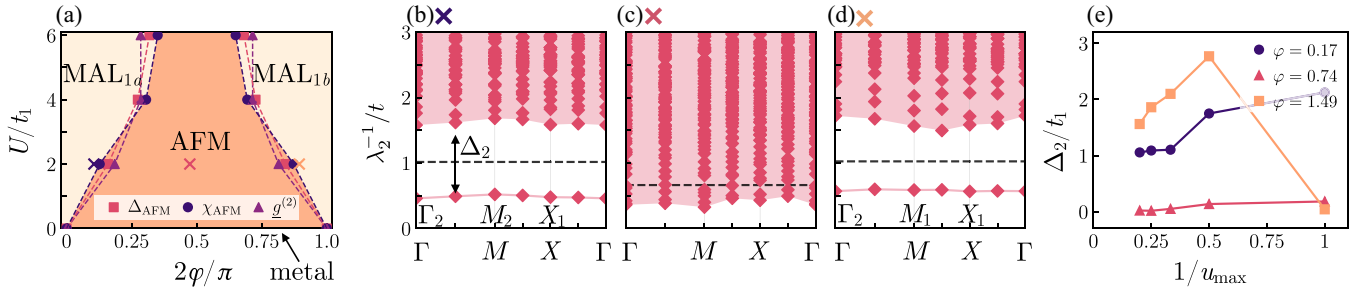


FIG. 8. Checkerboard lattice of Hubbard squares. (a) Phase diagram as a function of $\varphi/(\pi/2)$ and $U/t$ ($t_1 = t\cos\varphi,\ t_3 = t\sin\varphi$). The phase boundaries are evaluated using (i) $\Delta_{\rm AFM}$, the vanishing gap between the ground state and the $S = 1$ and $\boldsymbol{k} = (\pi, \pi)$ excited state, extrapolated for $L \to \infty$ from the QMC data; (ii) $\chi_{\rm AFM}$, the inflection point in susceptibility towards the Néel order, obtained within QMC on the $L = 5$ lattice (corresponding to $L \times L$ unit cells); and (iii) $\underline{g}^{(2)}$, the gap closing in the inverse spectra of $\underline{g}^{(2)}$, obtained in QMC for a system with $L = 3$ (see the SM [55]). The three crosses mark the points in the phase diagram corresponding to the (b)–(d) plots. [(b)–(d)] Inverted spectrum of $\underline{g}^{(2)}$ in the three regimes (b) $t_1 \gg t_3$ ($\varphi = 0.08$), (c) $t_1 \approx t_3$ ($\varphi = 0.74$), and (d) $t_1 \ll t_3$ ($\varphi = 1.49$), for $U/t = 2$ and $\varphi = \arctan(t_1/t_3)$. The spectra in (b)–(d) are evaluated with QMC, for a system of size $L = 4$. (e) Convergence of the spectral gap in the inverted spectrum of $\underline{g}^{(2)}$ as a function of inverse cluster size $1/u_{\rm max}$, for systems with $L = 4$ and $\varphi = 0.00,\ 0.17,\ 1.41,\ 1.57$.

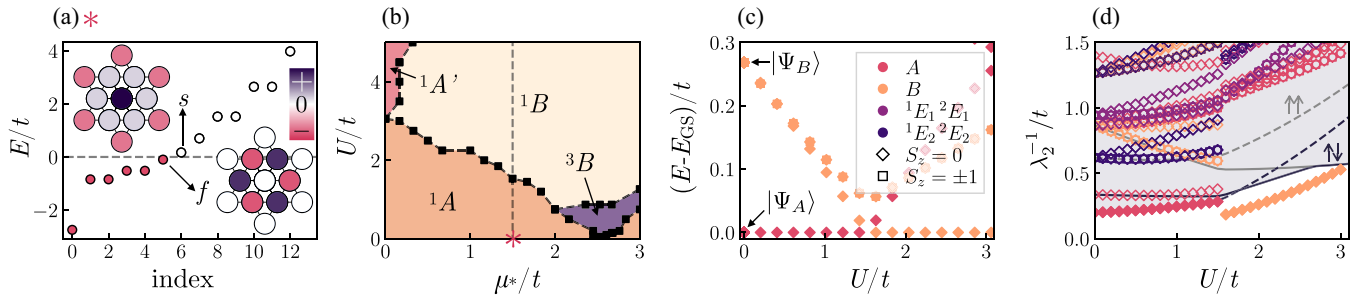


FIG. 9. Star of David. (a) Single-particle spectrum of the star of David at $U/t = 0$, $\mu_*/t = 1.5$. Each eigenvalue is doubly degenerate due to the spin degree of freedom. The two levels closest to zero energy correspond to the $s$ and $f$ states. Their wave function weights are shown in the insets. (b) Phase diagram obtained within ED of the star of David as a function of $\mu_*/t$ and $U/t$ in the Hilbert space of $N = 12$ electrons, at fixed $t'/t = 1$ and $t''/t = 0.4$. Phases are labeled by $^{2S+1}R$, where $R$ indicates the $C_6$ representation in which the ground state transforms and $S$ its total spin. (The representation labeled by $A$ corresponds to $A_1$ for $C_{6v}$, while $A'$ corresponds to $A_2$.) The pink asterisk marks the parameters of (a). (c) Low-energy spectrum at $N = 12$ as a function of $U$, plotted with respect to the lowest energy eigenvalue (i. e., the ground-state energy). (d) Inverted $g^{(2)}$ spectrum obtained in ED with a cutoff of $m_{\max} = 300$ in each symmetry sector as a function of $U$ (see the SM [55]). The lowest eigenvalues are colored according to the physical representation of $C_6$ in which their eigenstates transform. The continuous (dashed) lines mark the $N-2$ ($N+2$) many-body gap, $\Delta_{N\pm2} = E_{\min,N\pm2} - E_{GS,N}$ with $N = 12$. The gray (black) lines refer to excitations with $S_z = \pm1$ ($S_z = 0$). In (c)–(d), the parameters are $\mu_*/t = 1.5$, $t'/t = 1$, and $t''/t = 0.4$, corresponding to the dashed line in (b). The legend in (c) applies to both (c) and (d). In (d), only the lowest eigenvalues are filled with color, for visibility.

$T-TaS_2$, a cluster Mott insulator where the originally triangular lattice of each layer undergoes a charge density wave instability that leads to the formation of a star of David pattern [91,92]. While detailed theoretical models have been developed to discuss this system [85], here we present a simplified single-orbital model to analyze an individual cluster.

We consider the star of David cluster shown in Fig. 5(d), with a single trivial spinful orbital placed at each one of the thirteen sites. To distinguish between AL and MAL phases, a possible minimal symmetry group is the double group of $C_6$ (see Table S11 within the SM [55]). We consider a tight binding model with nearest-neighbor hoppings and on-site Hubbard interaction. In addition, we introduce a local chemical potential $\mu_*$ acting on the central site only, which is distinguished by an asterisk in Fig. 5(d). The model Hamiltonian for this star of David cluster reads

$$\begin{aligned}\hat{H} = &\sum_{i=1}^{13}\sum_{\sigma} t(\hat{c}^\dagger_{i,\sigma}\hat{c}_{i+1,\sigma} + \text{H.c.}) \\ &+ \sum_{i=1}^{6}\sum_{\sigma}[t'(\hat{c}^\dagger_{2i,\sigma}\hat{c}_{1,\sigma} + \text{H.c.}) + t''(\hat{c}^\dagger_{2i,\sigma}\hat{c}_{2i+2,\sigma} + \text{H.c.})] \\ &+ U\sum_{i=1}^{13}\hat{n}_{i,\uparrow}\hat{n}_{i,\downarrow} + \mu\sum_{i=1}^{13}\sum_{\sigma}\hat{n}_{i,\sigma} + \mu_*\sum_{\sigma}\hat{n}_{1,\sigma}, \quad (55)\end{aligned}$$

where we identified the sites $14 \equiv 2$, the parameters $t$, $t'$, and $t''$ describe the hopping amplitudes, $U$ the strength of the Hubbard interaction, $\mu$ the global chemical potential, and $\mu_*$ is the local chemical potential.

We focus on the case of electron filling $N = 12$, which allows for a TRS ground state, and we fix $t'/t = 1, t''/t = 0.4$. The regime of twelve electrons per star of David cluster may be reached experimentally upon sample doping. The phase diagram evaluated in ED as a function of $U$ and $\mu_*$ is shown in Fig. 9(b).

In the single-particle sector of the Hilbert space there are thirteen energy levels, each one twofold degenerate due to the spin degree of freedom. At $U = 0$, $\mu_* = 0$, and $N = 12$, these energy levels are filled up to some states, which we label by $f$, whose symmetry eigenvalue under sixfold rotation ($C_6$) is $-1$, see Fig 9(a). We define the creation operators for these states as $\hat{c}^\dagger_{f,\sigma}$, with $\sigma = \{\uparrow, \downarrow\}$. In this limit, the many-body ground state is a gapped AL, with the first twelve levels completely filled

$$|\Psi_A\rangle = \hat{c}^\dagger_{f,\uparrow}\hat{c}^\dagger_{f,\downarrow}|\Phi\rangle, \quad (56)$$

where $|\Phi\rangle$ indicates the many-body state where all the single-particle states with energy below the one of the $f$ states are completely filled. At the Fermi energy $-\mu$, there are two pairs of spin-degenerate single-particle states with $C_6$ eigenvalue $+1$ and $-1$ respectively. For finite values of $\mu_* > 0$, the spin-degenerate single-particle states at the Fermi energy characterized by $C_6$ eigenvalue $+1$, which we call $s$ states, become lower in energy, and eventually reach the $f$ energy value, for $\mu_*^c/t \sim 2.5$. We indicate creation operators that create electrons in the $s$ state by $\hat{c}^\dagger_{s,\sigma}$, $\sigma = \{\uparrow, \downarrow\}$. The inset of Fig. 9(a) shows the single-particle noninteracting spectrum at the value $\mu_*/t = 1.5$.

As $\mu_*$ and $U$ increase, the relevant low-energy sector of the Hilbert space at finite but small $U$ involves the states where all the levels with energy below the one of $f$ are filled, while the remaining two electrons occupy some of the $s$ and $f$ states. In the limit $U \to 0$ and $\mu_* < \mu_*^c$, the ground state remains the gapped AL of Eq. (56). For small but finite $U$, the ground state is adiabatically connected to the AL in Eq. (56), and it transforms in the $A$ representation of $C_6$. For larger values of $U$, the antiferromagnetic exchange favors the singlet configuration mixing the $s$ and $f$ states, leading to a level crossing in the many-body spectrum [see Fig. 9(c)]. After the crossing, the new many-body ground state is a gapped singly degenerate state that transforms in the $B$ representation of the point group, and has total spin zero. This ground state can be

adiabatically continued to the state

$$|\Psi_B\rangle = \frac{1}{\sqrt{2}}(\hat{c}^\dagger_{f,\uparrow}\hat{c}^\dagger_{s,\downarrow} - \hat{c}^\dagger_{f,\downarrow}\hat{c}^\dagger_{s,\uparrow})\,|\Phi\rangle\,, \tag{57}$$

which appears as an excited state in the many-body spectrum at $U \to 0$. The state in Eq. (57) is an MAL state, and from this we deduce that the ground state in the $B$ phase can be adiabatically connected to an MAL state.

We compute the spectrum of $\underline{g}^{(2)}$ for the star of David cluster in ED and by truncating the Hamiltonian (see the SM [55] for further details), keeping $\mu_*/t = 1.5$ fixed while varying $U$. Figure 9(d) shows the resulting inverted spectrum of $\underline{g}^{(2)}$. At values of $U$ lower that the critical interaction strength at which there is the transition between the $A$ phase and the $B$ phase, the lowest inverse eigenvalue of $\underline{g}^{(2)}$ transforms in the $A$ representation, and lies at the edge of the continuum of the spectrum. In the $B$ phase, there is a gap separation between the continuum of the inverse spectrum of $\underline{g}^{(2)}$ and a lowest-lying eigenvalue transforming in the $B$ representation. Therefore, for the star of David cluster one can distinguish between the AL phase, labeled by $A$, and the MAL phase, labeled by $B$, by looking at the spectrum of $\underline{g}^{(2)}$.

As seen in the cases of the Hubbard diamond chain (Sec. VI B) and the checkerboard lattice of Hubbard squares (Sec. VI C), weakly coupling several clusters that realize an MAL state results in an MAL phase that extends over the full lattice. This in principle will also apply to the case of the star of David clusters, which can then be diagnosed through the spectrum of $\underline{g}^{(2)}$ computed for the whole lattice.

## VII. CONCLUSIONS

Topological quantum chemistry is a framework for classifying materials based on the single-particle band structure developed with noninteracting electrons in mind. In particular, TQC lists all possible AL states for a given space group and compares a given first principles band structure to the respective list. If the band structure can not be constructed from an AL, it is said to be topological. While it is possible to apply the tools of TQC to interacting materials by using the (inverse of the) one-particle Green's function as an effective Hamiltonian, such an approach is blind to much of the richness of interacting states.

Electronic interactions are important in many materials of interest and may drive a system into a state that is not adiabatically connected to a noninteracting state. It is for this setting that the framework of iTQC provides new insights through the symmetry properties of the many-body Green's function. Consequently, while TQC naturally works "from first principles", in other words the analytic result of classifying AL-induced band structures is compared to bands obtained from density functional theory, the starting point of iTQC is inherently an interacting electron system. A natural testing ground for iTQC, which we discussed in this paper, are thus toy models of interacting electrons on a given lattice. Still, such models can in principle be obtained from first principles through, e. g., via constrained RPA [93,94] or the linear response approach [95,96].

The basic building block of iTQC's trial states is the $n$-MAL operator, which creates a cluster of $n$-electrons with nontrivial transformation properties under spatial symmetries. They are 0D-block cSPTs, including classes of cSPTs that are disconnected from any noninteracting state. Existing frameworks to identify the nature of entangled and featureless many-body states typically rely on nonlocal observables like string-order parameters [70] or entanglement spectra [97] that are hard to access in traditional condensed matter experiments. A strength of the Green's function based iTQC formalism is that it is based on substantially less exotic correlation functions that could be measurable. In ED, there is no computational gain from using our method. Yet, in QMC and in quantum simulations the type of correlators we consider are generically easier to compute than SPT topological invariants. Therefore for most physically relevant cases, the recipe proposed in the present paper is comparatively computationally cheaper. Specifically, it is possible to infer information about the particle-particle Green's function $\underline{g}^{(2)}$ by relating it to the superconducting susceptibility

$$\chi_{\alpha\beta\gamma\delta}(\boldsymbol{q},\tau) = \sum_{\boldsymbol{k},\boldsymbol{k}'}\langle T_\tau \hat{c}^\dagger_{\boldsymbol{k}-\boldsymbol{q},\alpha}(\tau)\hat{c}^\dagger_{-\boldsymbol{k},\beta}(\tau)\hat{c}_{\boldsymbol{k}'+\boldsymbol{q},\gamma}(0)\hat{c}_{-\boldsymbol{k}',\delta}(0)\rangle, \tag{58}$$

where $T_\tau$ is the time-ordering operator [98]. However, in experiments it may be easier to measure the particle-hole Green's function $\underline{g}^{(2)}_{\rm ph}$. For example, in neutron scattering one measures the spin-spin correlation function and certain electromagnetic properties are related to the current-current correlator, which can be computed from $\underline{g}^{(2)}_{\rm ph}$ [99]. Furthermore, Raman scattering cross sections depend on $\underline{g}^{(2)}_{\rm ph}$ [100]. A measurement of the anticorrelation of electrons in momentum space can show the "correlation hole" originating from the Pauli principle and repulsive Coulomb interactions [101,102]. Alternatively, one can observe the two-photon two-electron spectra with intense pulses of light [103].

While we have focused in this paper entirely on the case of $n = 1$ and $n = 2$, in other words ALs and 2-MALs, the generalization to higher $n$-MALs is in principle straight forward in the iTQC formalism and is a possible extension of our current paper. To do so, one would consider the correlation functions $\langle \hat{O}^\dagger(t), \hat{O}(0)\rangle$, where $\hat{O}^\dagger$ is a $n$-particle operator, and there is a single bosonic or fermionic time, for $n$-even or $n$-odd respectively. Still, the computational complexity of the Green's functions increases with $n$ and therefore—in the absence of an efficient numerical scheme to evaluate many-body Green's functions—this approach is likely to be useful only for small $n$. Focusing on small $n$ is equivalent to a truncation in the entanglement entropy of the states we study, therefore it is likely that tensor network states are a natural language in which to think about this problem. Using tensor networks, one can obtain the $\underline{g}^{(2)}$ band structures for a larger class of model systems, including topological ones, to diagnose their properties.

In this paper, we focused on the MAL-induced bandstructures of the two-particle Green's function; however, fragile topological phases also have signatures appearing in the Cooper pair spectrum [104] and should therefore be amenable to our approach. We leave the full extension of our scheme to fragile phases to future work.

Another important future goal is the application of iTQC to real materials. Given the finite size of the clusters we consider, any crystal structure that already has a natural substructure would be well suited for a realization of the topological analysis we are presenting. A possible candidate is for example Y-kapellasite [105] whose underlying lattice structure is that of hexagonal clusters of Cu $3d^9$ atoms arranged in a triangular lattice.

## ACKNOWLEDGMENTS

We thank the authors of Ref. [106] for sharing an advance copy of their preprint. We would like to thank B. A. Bernevig, J. Arbeitman-Herzog, J. C. Wang, K. Shiozaki, X. Dai, F. Pollmann, A. Fünfhaus, and J. L. Mañes for useful discussions. G.W. acknowledges NCCR MARVEL funding from the Swiss National Science Foundation. M.O.S. and T.N. acknowledge funding from the Swiss National Science Foundation (Project No. 200021E_198011) as part of the QUAST FOR 5249-449872909 (Project P3). R.V. and M.G.V. acknowledge support from the Deutsche Forschungsgemeinschaft (DFG, German Research Foundation) through QUAST FOR 5249-449872909 (Project P4) and M.G.V. thanks European Research Council (ERC) Grant Agreement No. 101020833. M.G.V. and M.I. acknowledge Spanish Ministerio de Ciencia e Innovacion (Grant No. PID2019-109905GBC21). A.T. is supported by the Swedish Research Council (VR) through Grants No. 2019-04736 and No. 2020-00214. Exact diagonalization was performed using the `quspin` package [107]. The QMC and ED simulations were supported by the RSF Grant (Project No. 21-12-00237) and used the computing resources of the federal collective usage center "Complex for simulation and data processing for mega-science facilities" at NRC "Kurchatov Institute".

[1] K. v. Klitzing, G. Dorda, and M. Pepper, New Method for High-Accuracy Determination of the Fine-Structure Constant Based on Quantized Hall Resistance, Phys. Rev. Lett. **45**, 494 (1980).

[2] C. L. Kane and E. J. Mele, Quantum Spin Hall Effect in Graphene, Phys. Rev. Lett. **95**, 226801 (2005).

[3] C. L. Kane and E. J. Mele, $Z_2$ Topological Order and the Quantum Spin Hall Effect, Phys. Rev. Lett. **95**, 146802 (2005).

[4] M. Z. Hasan and C. L. Kane, Colloquium: Topological insulators, Rev. Mod. Phys. **82**, 3045 (2010).

[5] M. Sato and Y. Ando, Topological superconductors: A review, Rep. Prog. Phys. **80**, 076501 (2017).

[6] B. A. Bernevig, T. L. Hughes, and S.-C. Zhang, Quantum spin Hall effect and topological phase transition in HgTe quantum wells, Science **314**, 1757 (2006).

[7] L. Fu, C. L. Kane, and E. J. Mele, Topological Insulators in Three Dimensions, Phys. Rev. Lett. **98**, 106803 (2007).

[8] M. Konig, S. Wiedmann, C. Brüne, A. Roth, H. Buhmann, L. W. Molenkamp, X.-L. Qi, and S.-C. Zhang, Quantum spin Hall insulator state in HgTe quantum wells, Science **318**, 766 (2007).

[9] D. Hsieh, D. Qian, L. Wray, Y. Xia, Y. S. Hor, R. J. Cava, and M. Z. Hasan, A topological Dirac insulator in a quantum spin Hall phase, Nature (London) **452**, 970 (2008).

[10] A. P. Schnyder, S. Ryu, A. Furusaki, and A. W. W. Ludwig, Advances in the oretical physics: Landau memorial conference, AIP Conf. Proc. **1134**, 10 (2009).

[11] S. Ryu, A. P. Schnyder, A. Furusaki, and A. W. W. Ludwig, Topological insulators and superconductors: Tenfold way and dimensional hierarchy, New J. Phys. **12**, 065010 (2010).

[12] L. Fu, Topological Crystalline Insulators, Phys. Rev. Lett. **106**, 106802 (2011).

[13] H. C. Po, H. Watanabe, and A. Vishwanath, Fragile Topology and Wannier Obstructions, Phys. Rev. Lett. **121**, 126402 (2018).

[14] Z. Wang, B. J. Wieder, J. Li, B. Yan, and B. A. Bernevig, Higher-Order Topology, Monopole Nodal Lines, and the Origin of Large Fermi Arcs in Transition Metal Dichalcogenides $XTe_2$ ($X$ = Mo, W), Phys. Rev. Lett. **123**, 186401 (2019).

[15] A. Bouhon, T. c. v. Bzdušek, and R.-J. Slager, Geometric approach to fragile topology beyond symmetry indicators, Phys. Rev. B **102**, 115135 (2020).

[16] A. Nelson, T. Neupert, A. Alexandradinata, and T. Bzdušek, Delicate topology protected by rotation symmetry: Crystalline Hopf insulators and beyond, Phys. Rev. B **106**, 075124 (2022).

[17] S. A. Díaz, J. Klinovaja, and D. Loss, Topological Magnons and Edge States in Antiferromagnetic Skyrmion Crystals, Phys. Rev. Lett. **122**, 187203 (2019).

[18] A. Corticelli, R. Moessner, and P. A. McClarty, Identifying and Constructing Complex Magnon Band Topology, Phys. Rev. Lett. **130**, 206702 (2023).

[19] T. Van Mechelen, S. Bharadwaj, Z. Jacob, and R.-J. Slager, Optical $n$-insulators: Topological obstructions to optical Wannier functions in the atomistic susceptibility tensor, Phys. Rev. Res. **4**, 023011 (2022).

[20] H. C. Po, A. Vishwanath, and H. Watanabe, Symmetry-based indicators of band topology in the 230 space groups, Nat. Commun. **8**, 50 (2017).

[21] H. C. Po, Symmetry indicators of band topology, J. Phys.: Condens. Matter **32**, 263001 (2020).

[22] B. Bradlyn, L. Elcoro, J. Cano, M. G. Vergniory, Z. Wang, C. Felser, M. I. Aroyo, and B. A. Bernevig, Topological quantum chemistry, Nature (London) **547**, 298 (2017).

[23] M. Vergniory, L. Elcoro, C. Felser, N. Regnault, B. A. Bernevig, and Z. Wang, A complete catalogue of high-quality topological materials, Nature (London) **566**, 480 (2019).

[24] J. Cano and B. Bradlyn, Band representations and topological quantum chemistry, Annu. Rev. Condens. Matter Phys. **12**, 225 (2021).

[25] L. Elcoro, B. J. Wieder, Z. Song, Y. Xu, B. Bradlyn, and B. A. Bernevig, Magnetic topological quantum chemistry, Nat. Commun. **12**, 5965 (2021).

[26] J. Kruthoff, J. de Boer, J. van Wezel, C. L. Kane, and R.-J. Slager, Topological Classification of Crystalline Insulators through Band Structure Combinatorics, Phys. Rev. X **7**, 041069 (2017).

[27] J. Zak, Band representations of space groups, Phys. Rev. B **26**, 3010 (1982).

[28] L. Michel and J. Zak, Connectivity of energy bands in crystals, Phys. Rev. B **59**, 5998 (1999).

[29] Y. Chen, S.-J. Huang, Y.-T. Hsu, and T.-C. Wei, Topological invariants beyond symmetry indicators: Boundary diagnostics for twofold rotationally symmetric superconductors, Phys. Rev. B **105**, 094518 (2022).

[30] J. Cano, L. Elcoro, M. I. Aroyo, B. A. Bernevig, and B. Bradlyn, Topology invisible to eigenvalues in obstructed atomic insulators, Phys. Rev. B **105**, 125115 (2022).

[31] S. Rachel, Interacting topological insulators: A review, Rep. Prog. Phys. **81**, 116501 (2018).

[32] J. Wen, A. Ruegg, C.-C. J. Wang, and G. A. Fiete, Interaction-driven topological insulators on the kagome and the decorated honeycomb lattices, Phys. Rev. B **82**, 075125 (2010).

[33] X. Chen, Z.-C. Gu, Z.-X. Liu, and X.-G. Wen, Symmetry-protected topological orders in interacting bosonic systems, Science **338**, 1604 (2012).

[34] J. M. McKay and V. E. Henrich, Structure of Valence and Conduction Levels in NiO, Phys. Rev. Lett. **53**, 2343 (1984).

[35] J. van Elp, R. H. Potze, H. Eskes, R. Berger, and G. A. Sawatzky, Electronic structure of MnO, Phys. Rev. B **44**, 1530 (1991).

[36] G. Trimarchi, Z. Wang, and A. Zunger, Polymorphous band structure model of gapping in the antiferromagnetic and paramagnetic phases of the Mott insulators MnO, FeO, CoO, and NiO, Phys. Rev. B **97**, 035107 (2018).

[37] J. A. Wilson and G. D. Pitt, Metal-insulator transition in $NiS_2$, Philos. Mag. **23**, 1297 (1971).

[38] A previously proposed interacting TQC extension is limited to states adiabatically connected to noninteracting ones [54,75].

[39] F. Becca and S. Sorella, *Quantum Monte Carlo Approaches for Correlated Systems* (Cambridge University Press, Cambridge 2017) p. 272.

[40] R. J. Bartlett and M. Musiał, Coupled-cluster theory in quantum chemistry, Rev. Mod. Phys. **79**, 291 (2007).

[41] X.-G. Wen, Colloquium: Zoo of quantum-topological phases of matter, Rev. Mod. Phys. **89**, 041004 (2017).

[42] T. Senthil, Symmetry-protected topological phases of quantum matter, Annu. Rev. Condens. Matter Phys. **6**, 299 (2015).

[43] S.-J. Huang, H. Song, Y.-P. Huang, and M. Hermele, Building crystalline topological phases from lower-dimensional states, Phys. Rev. B **96**, 205106 (2017).

[44] H. Song, S.-J. Huang, L. Fu, and M. Hermele, Topological Phases Protected by Point Group Symmetry, Phys. Rev. X **7**, 011020 (2017).

[45] Z. Song, S.-J. Huang, Y. Qi, C. Fang, and M. Hermele, Topological states from topological crystals, Sci. Adv. **5**, eaax2007 (2019).

[46] Z. Song, C. Fang, and Y. Qi, Real-space recipes for general topological crystalline states, Nat. Commun. **11**, 4197 (2020).

[47] J.-H. Zhang, S. Yang, Y. Qi, and Z.-C. Gu, Real-space construction of crystalline topological superconductors and insulators in 2D interacting fermionic systems, Phys. Rev. Res. **4**, 033081 (2022).

[48] C.-C. Chen, L. Muechler, R. Car, T. Neupert, and J. Maciejko, Fermionic Symmetry-Protected Topological Phase in a Two-Dimensional Hubbard Model, Phys. Rev. Lett. **117**, 096405 (2016).

[49] D. Pesin and L. Balents, Mott physics and band topology in materials with strong spin–orbit interaction, Nat. Phys. **6**, 376 (2010).

[50] I. F. Herbut and L. Janssen, Topological Mott Insulator in Three-Dimensional Systems with Quadratic Band Touching, Phys. Rev. Lett. **113**, 106401 (2014).

[51] M. Bijelic, R. Kaneko, C. Gros, and R. Valentí, Suppression of topological Mott-Hubbard phases by multiple charge orders in the honeycomb extended Hubbard model, Phys. Rev. B **97**, 125142 (2018).

[52] P. Mai, B. Feldman, and P. W. Phillips, Topological Mott insulator at quarter filling in the interacting Haldane Model, Phys. Rev. Res. **5**, 013162 (2022).

[53] H. Yao and S. A. Kivelson, Fragile Mott Insulators, Phys. Rev. Lett. **105**, 166402 (2010).

[54] M. Iraola, N. Heinsdorf, A. Tiwari, D. Lessnich, T. Mertz, F. Ferrari, M. H. Fischer, S. M. Winter, F. Pollmann, T. Neupert, R. Valentí, and M. G. Vergniory, Towards a topological quantum chemistry description of correlated systems: The case of the Hubbard diamond chain, Phys. Rev. B **104**, 195125 (2021).

[55] See Supplemental Material at http://link.aps.org/supplemental/10.1103/PhysRevB.107.245145 for details on the Mott atomic limit properties, two-particle Green's functions calculations in the limit of spectrally flattened many body Hamiltonian, and numerical calculations whose results are discussed in the main text. The Supplemental Material also contains Refs. [56–59].

[56] T. Hahn, ed., *International Tables for Crystallography. Volume A: Space-group symmetry* (Springer, New York, 2005).

[57] F. F. Assaad, M. Imada, and D. J. Scalapino, Charge and spin structures of a $d_{x^2-y^2}$ superconductor in the proximity of an antiferromagnetic Mott insulator, Phys. Rev. B **56**, 15001 (1997).

[58] C. Bradley and A. Cracknell, *Mathematical Theory of Symmetry in Solids* (Clarendon Press, Oxford, 1972).

[59] A. P. Cracknell, B. L. Davies, S. C. Miller, and W. F. Love, *Kronecher Product Tables, 1, General Introduction and Tables of Irreducible Representations of Space groups* (Clarendon Press, Oxford, 1979).

[60] P. Anderson, Resonating valence bonds: A new kind of insulator? Mater. Res. Bull. **8**, 153 (1973).

[61] A more general notion of an MAL is possible, where the cluster operators overlap. Such states include resonant valence bond states as the $S'$-Mott phase of the Hubbard ladder [62]. We leave this extension to future work.

[62] M. Tsuchiizu and A. Furusaki, Generalized two-leg Hubbard ladder at half filling: Phase diagram and quantum criticalities, Phys. Rev. B **66**, 245106 (2002).

[63] We are interested in symmetries, which map the 1D system back to itself, but reverse its one spatial coordinate axis. Another symmetry, which does this is two-fold rotation about an axis perpendicular to the 1D system. We do not separately discuss it here as it has the same representation as mirror symmetry.

[64] The set of orbitals placed at each $2c$ Wyckoff position transforms in the $\bar{A}\bar{A}$ physical representation of the double site symmetry group 1. According to the notation introduced above, the $\alpha$ index labeling these operators reads $\hat{c}^{\dagger}_{r,\alpha} :=$

$\hat{c}^{\dagger}_{r,2c,a,\bar{A}\bar{A},\sigma}$, with $a \in \{1,2\}$ and $\sigma \in \{\uparrow,\downarrow\}$, where we use a spin label to indicate a realization of TRS states. In the main text, we suppress the $2c$ and $\bar{A}\bar{A}$ labels for the sake of simplicity.

[65] Although it is enough to consider the more general case of cSPTs, here we also explicitly refer to pgSPTs as the results presented later on in the section were derived in the context of pgSPTs. For the latter, the classification is based on a point group rather than the full space group. Although less refined, the pgSPT case is sufficient to convey the key concepts of the cSPT classification.

[66] K. Shiozaki, H. Shapourian, and S. Ryu, Many-body topological invariants in fermionic symmetry-protected topological phases: Cases of point group symmetries, Phys. Rev. B **95**, 205139 (2017).

[67] H. Shapourian, K. Shiozaki, and S. Ryu, Many-Body Topological Invariants for Fermionic Symmetry-Protected Topological Phases, Phys. Rev. Lett. **118**, 216402 (2017).

[68] R. Thorngren and D. V. Else, Gauging Spatial Symmetries and the Classification of Topological Crystalline Phases, Phys. Rev. X **8**, 011040 (2018).

[69] K. Shiozaki, H. Shapourian, K. Gomi, and S. Ryu, Many-body topological invariants for fermionic short-range entangled topological phases protected by antiunitary symmetries, Phys. Rev. B **98**, 035151 (2018).

[70] F. Pollmann and A. M. Turner, Detection of symmetry-protected topological phases in one dimension, Phys. Rev. B **86**, 125441 (2012).

[71] X.-L. Qi, T. L. Hughes, and S.-C. Zhang, Topological field theory of time-reversal invariant insulators, Phys. Rev. B **78**, 195424 (2008).

[72] V. Gurarie, Single-particle Green's functions and interacting topological insulators, Phys. Rev. B **83**, 085426 (2011).

[73] Z. Wang and S.-C. Zhang, Simplified Topological Invariants for Interacting Insulators, Phys. Rev. X **2**, 031008 (2012).

[74] Z. Wang and B. Yan, Topological Hamiltonian as an exact tool for topological invariants, J. Phys.: Condens. Matter **25**, 155601 (2013).

[75] D. Lessnich, S. M. Winter, M. Iraola, M. G. Vergniory, and R. Valentí, Elementary band representations for the single-particle Green's function of interacting topological insulators, Phys. Rev. B **104**, 085116 (2021).

[76] Z. Wang, X.-L. Qi, and S.-C. Zhang, Topological invariants for interacting topological insulators with inversion symmetry, Phys. Rev. B **85**, 165126 (2012).

[77] N. Wagner, L. Crippa, A. Amaricci, P. Hansmann, M. Klett, E. König, T. Schäfer, D. Di Sante, J. Cano, A. Millis, A. Georges, and G. Sangiovanni, Mott insulators with boundary zeros, arXiv:2301.05588.

[78] N. N. Bogoliubov, Kinetic equations, Zh. Eksp. Teor. Fiz. **16**, 691 (1946) [Sov. Phys. JETP **10**, 265 (1946)].

[79] H. Bruus and K. Flensberg, *Many-body quantum theory in condensed matter physics - An introduction* (Oxford University Press, New York, 2004).

[80] A. Kitaev, Periodic table for topological insulators and superconductors, AIP Conf. Proc. **1134**, 22 (2009).

[81] Here we set $\boldsymbol{u} = \boldsymbol{0}$ in the AL and MAL states proposed, with $\boldsymbol{u}$ as introduced Eq. (3). It is for this reason that $u_{\max} = 0$ is sufficient to capture the relevant correlations of the MAL state in Eq. (34).

[82] W. P. Su, J. R. Schrieffer, and A. J. Heeger, Solitons in Polyacetylene, Phys. Rev. Lett. **42**, 1698 (1979).

[83] L. Elcoro, B. Bradlyn, Z. Wang, M. G. Vergniory, J. Cano, C. Felser, B. A. Bernevig, D. Orobengoa, G. de la Flor, and M. I. Aroyo, Double crystallographic groups and their representations on the Bilbao Crystallographic server, J. Appl. Crystallogr. **50**, 1457 (2017).

[84] We denote by $\bar{A}_1\bar{A}_2$ the physical irrep that realizes TRS, constructed out of the two irreducible representations $\bar{A}_1$, $\bar{A}_2$ of a certain point group $G_{\boldsymbol{x}}$. These physical representations are the corepresentations of the magnetic point group constructed as $G_{\boldsymbol{x}} + \mathcal{T}G_{\boldsymbol{x}}$, which is a type-II magnetic group.

[85] S. Qiao, X. Li, N. Wang, W. Ruan, C. Ye, P. Cai, Z. Hao, H. Yao, X. Chen, J. Wu, Y. Wang, and Z. Liu, Mottness Collapse in $1T-TaS_{2-x}Se_x$ Transition-Metal Dichalcogenide: An Interplay between Localized and Itinerant Orbitals, Phys. Rev. X **7**, 041054 (2017).

[86] D. J. Scalapino and S. A. Trugman, Local antiferromagnetic correlations and $d_{x^2-y^2}$ pairing, Phil. Mag. B **74**, 607 (1996).

[87] R. Schumann, Thermodynamics of a 4-site Hubbard model by analytical diagonalization, Ann. Physik **514**, 49 (2002).

[88] S. Chakravarty and S. A. Kivelson, Electronic mechanism of superconductivity in the cuprates, $C_{60}$, and polyacenes, Phys. Rev. B **64**, 064511 (2001).

[89] For each site of the Hubbard square, the only symmetry leaving the site invariant is the diagonal mirror operation passing through the site. Hence, the site symmetry group of each of the sites at the corner is the double group of $C_s$. A spinful orbital transforming in the spinful trivial physical representation $({}^1\bar{E}\,{}^2\bar{E})$ of the double group of $C_s$ is placed at each site of the square (see Table S10 within the SM [55]). This corresponds to a spin-1/2 with quantization axis along the out-of-plane direction.

[90] L. Muechler, J. Maciejko, T. Neupert, and R. Car, Möbius molecules and fragile Mott insulators, Phys. Rev. B **90**, 245142 (2014).

[91] P. Fazekas and E. Tosatti, Electrical, structural and magnetic properties of pure and doped 1T-TaS2, Phil. Mag. B **39**, 229 (1979).

[92] K. T. Law and P. A. Lee, $1T-TaS_2$ as a quantum spin liquid, Proc. Natl. Acad. Sci. USA **114**, 6996 (2017).

[93] F. Aryasetiawan, M. Imada, A. Georges, G. Kotliar, S. Biermann, and A. I. Lichtenstein, Frequency-dependent local interactions and low-energy effective models from electronic structure calculations, Phys. Rev. B **70**, 195104 (2004).

[94] F. Aryasetiawan, K. Karlsson, O. Jepsen, and U. Schönberger, Calculations of Hubbard $U$ from first-principles, Phys. Rev. B **74**, 125106 (2006).

[95] M. Cococcioni and S. de Gironcoli, Linear response approach to the calculation of the effective interaction parameters in the LDA + U method, Phys. Rev. B **71**, 035105 (2005).

[96] G. C. Moore, M. K. Horton, A. M. Ganose, M. Siron, and K. A. Persson, High-throughput determination of Hubbard $U$ and Hund $J$ values for transition metal oxides via linear response formalism, arXiv:2201.04213.

[97] H. Li and F. D. M. Haldane, Entanglement Spectrum as a Generalization of Entanglement Entropy: Identification of Topological Order in Non-Abelian Fractional Quantum Hall Effect States, Phys. Rev. Lett. **101**, 010504 (2008).

[98] The superconducting susceptibility is thus related to the time-ordered Green's function, as opposed to the retarded Green's function considered in this paper.

[99] P. C. Martin and J. Schwinger, Theory of many-particle systems. I, Phys. Rev. **115**, 1342 (1959).

[100] C. M. Canali and S. M. Girvin, Theory of Raman scattering in layered cuprate materials, Phys. Rev. B **45**, 7127 (1992).

[101] F. O. Schumann, C. Winkler, G. Kerherve, and J. Kirschner, Mapping the electron correlation in two-electron photoemission, Phys. Rev. B **73**, 041404(R) (2006).

[102] F. O. Schumann, C. Winkler, and J. Kirschner, Correlation Effects in Two Electron Photoemission, Phys. Rev. Lett. **98**, 257604 (2007).

[103] J. Feist, S. Nagele, R. Pazourek, E. Persson, B. I. Schneider, L. A. Collins, and J. Burgdörfer, Probing Electron Correlation via Attosecond xuv Pulses in the Two-Photon Double Ionization of Helium, Phys. Rev. Lett. **103**, 063002 (2009).

[104] J. Herzog-Arbeitman, A. Chew, K.-E. Huhtinen, P. Törmä, and B. A. Bernevig, Many-body superconductivity in topological flat bands, arXiv:2209.00007.

[105] M. Hering, F. Ferrari, A. Razpopov *et al.*, Phase diagram of a distorted kagome antiferromagnet and application to Y-kapellasite, npj Comput. Mater. **8**, 10 (2022).

[106] J. Herzog-Arbeitman, B. A. Bernevig, and Z.-D. Song, Interacting topological quantum chemistry in 2D: Many-body real space invariants, arXiv:2212.00030.

[107] P. Weinberg and M. Bukov, QuSpin: A python package for dynamics and exact diagonalisation of quantum many body systems Part I: Spin chains, SciPost Phys. **2**, 003 (2017).